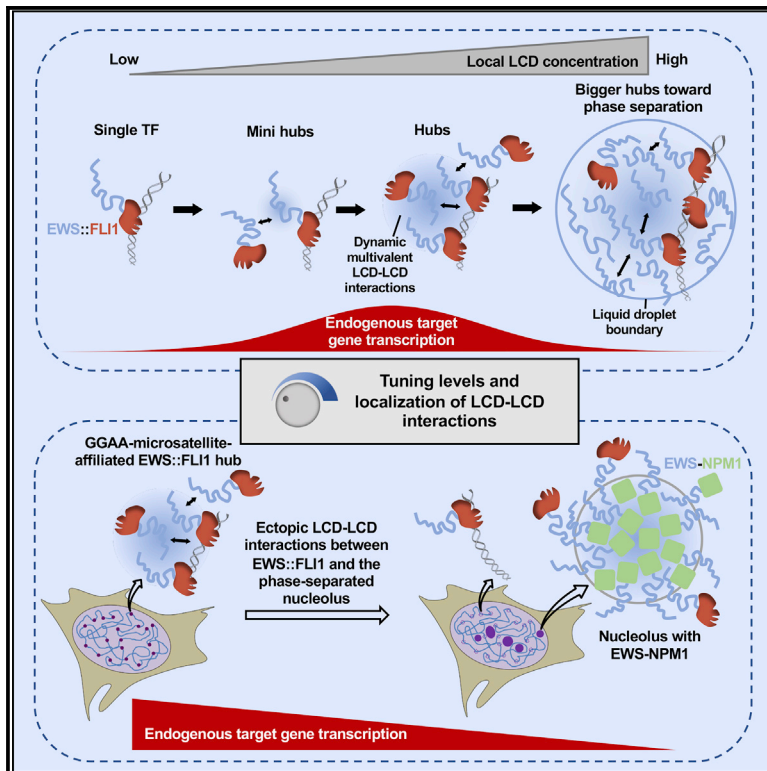


Tuning levels of low-complexity domain interactions to modulate endogenous oncogenic transcription

Graphical abstract



Authors

Shasha Chong, Thomas G.W. Graham, Claire Dugast-Darzacq, Gina M. Dailey, Xavier Darzacq, Robert Tjian

Correspondence

jmlim@berkeley.edu

In brief

It has been proposed that mammalian TFs require phase separation to activate transcription. Using EWS::FLI1 as a model system, Chong et al. show that a TF requires a narrow optimum of LCD-LCD interactions to activate transcription *in vivo*, and phase separation of TFs represses transcription of its endogenous target genes.

Highlights

- EWS::FLI1 requires a narrow optimum of LCD-LCD interactions to activate transcription
- Boosting LCD-LCD interactions toward phase separation represses transcription
- Sequestering EWS::FLI1 into the nucleolus inhibits its transcription functions
- EWS::FLI1 diffuses more slowly within the phase-separated nucleolus



Article

Tuning levels of low-complexity domain interactions to modulate endogenous oncogenic transcription

Shasha Chong,¹ Thomas G.W. Graham,² Claire Dugast-Darzacq,^{2,5} Gina M. Dailey,^{2,5} Xavier Darzacq,^{2,5} and Robert Tjian^{2,3,4,5,6,*}

¹Division of Chemistry and Chemical Engineering, California Institute of Technology, Pasadena, CA 91125, USA

²Department of Molecular and Cell Biology, University of California, Berkeley, Berkeley, CA 94720, USA

³Howard Hughes Medical Institute, University of California, Berkeley, Berkeley, CA 94720, USA

⁴Li Ka Shing Center for Biomedical & Health Sciences, University of California, Berkeley, Berkeley, CA 94720, USA

⁵CIRM Center of Excellence, University of California, Berkeley, Berkeley, CA 94720, USA

⁶Lead contact

*Correspondence: jmlim@berkeley.edu

<https://doi.org/10.1016/j.molcel.2022.04.007>

SUMMARY

Gene activation by mammalian transcription factors (TFs) requires multivalent interactions of their low-complexity domains (LCDs), but how such interactions regulate transcription remains unclear. It has been proposed that extensive LCD-LCD interactions culminating in liquid-liquid phase separation (LLPS) of TFs is the dominant mechanism underlying transactivation. Here, we investigated how tuning the amount and localization of LCD-LCD interactions *in vivo* affects transcription of endogenous human genes. Quantitative single-cell and single-molecule imaging reveals that the oncogenic TF EWS::FLI1 requires a narrow optimum of LCD-LCD interactions to activate its target genes associated with GGAA microsatellites. Increasing LCD-LCD interactions toward putative LLPS represses transcription of these genes in patient-derived cells. Likewise, ectopically creating LCD-LCD interactions to sequester EWS::FLI1 into a well-documented LLPS compartment, the nucleolus, inhibits EWS::FLI1-driven transcription and oncogenic transformation. Our findings show how altering the balance of LCD-LCD interactions can influence transcriptional regulation and suggest a potential therapeutic strategy for targeting disease-causing TFs.

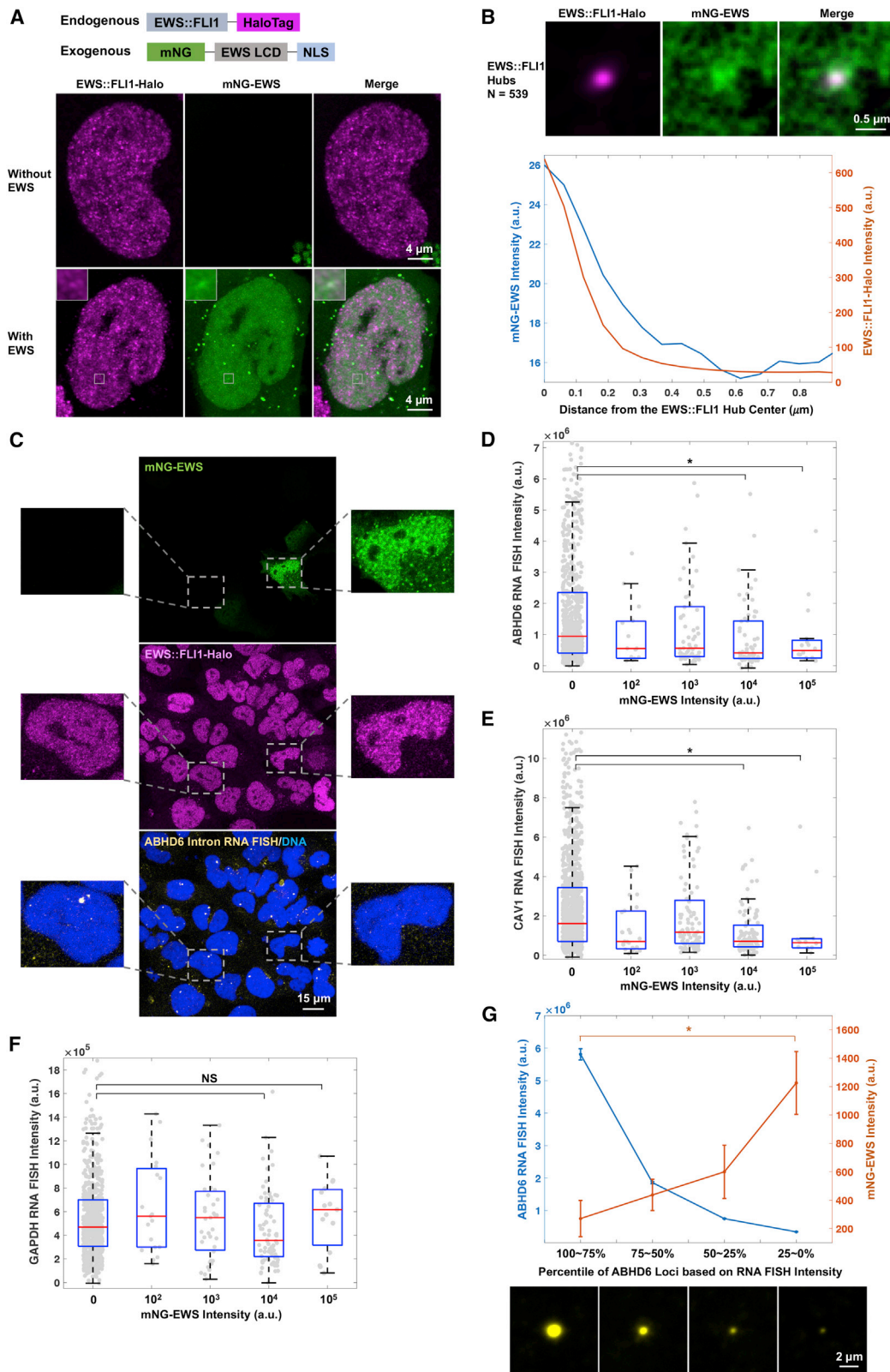
INTRODUCTION

Transcription is regulated by transcription factors (TFs), which contain DNA-binding and transactivation domains. DNA-binding domains usually have well-defined protein structures and recognize specific DNA sequences in a “lock-and-key” manner with precise stoichiometries (Kadonaga et al, 1988; Oka et al, 2004). In contrast, transactivation domains typically contain low-complexity domains (LCDs) that are intrinsically disordered and not amenable to conventional structure-function analysis. Recent advances in quantitative live-cell imaging revealed that dynamic, multivalent, and selective interactions occur between various TF LCDs and other intrinsically disordered regions found in the RNA polymerase II (Pol II) transcription machinery and associated cofactors (Boehning et al, 2018; Cho et al, 2018; Guo et al, 2019; Kwon et al, 2013; Sabari et al, 2018). These multivalent interactions help enrich TFs and other transcription regulators at specific genomic loci to form dynamic protein assemblies that we and others referred to as LCD-mediated “hubs” (Chong et al, 2018; Dufourt et al, 2018; Mir et al, 2017, 2018). Under certain conditions, LCD overexpression can induce

small transient hubs to develop properties resembling those of droplets/condensates formed via liquid-liquid phase separation (LLPS). LLPS has recently been invoked as a mechanism underlying numerous biological processes, including transcriptional regulation. However, most studies have employed *in vitro* or overexpression experiments to observe the formation of condensates and characterize their properties, while the physiological function of condensates *in vivo* remains poorly understood (McSwiggen et al., 2019b). Although it is clear that dynamic multivalent LCD-LCD interactions underlying both hub formation and LLPS could play a role in transactivation (Boehning et al, 2018; Bojja et al, 2018; Cho et al, 2018; Guo et al, 2019; Henninger et al, 2021; Hnisz et al, 2017; Kwon et al, 2013; Sabari et al, 2018), a causal link between LLPS and transactivation has remained elusive.

New questions have emerged from studying the effect of manipulating LCD-LCD interactions on transcription. Two recent papers reported that light-induced LLPS of TF LCDs increases global cellular transcription as well as transcription of a reporter gene within a transiently transfected plasmid (Schneider et al, 2021; Wei et al, 2020). In contrast, another manuscript reported





(legend on next page)

that although multivalent interactions of TF LCDs increase transcription of a synthetic gene array, LLPS of the LCDs did not further enhance expression (Trojanowski et al, 2021). These intriguing but conflicting findings motivated us to investigate the impact of tuning LCD-LCD interactions and inducing LLPS on transcription of specific endogenous genes with quantitative single-cell and single-molecule imaging. Our findings support a model where a TF requires finely tuned optimal levels of LCD-LCD interactions to activate its endogenous target genes, revealing new principles underlying LCD-interaction-mediated transactivation.

RESULTS

Enhanced levels of EWS LCD self-interactions repress EWS::FLI1-driven transcription

We focused on the oncogenic TF EWS::FLI1 that causes Ewing sarcoma. EWS::FLI1 is a fusion TF consisting of a transactivating LCD from EWSR1 (EWS LCD) and a DNA-binding domain from FLI1 that specifically recognizes the GGAA sequence. Recent studies showed that EWS::FLI1 forms local high-concentration hubs at GGAA microsatellites, highly repetitive GGAA-containing elements in the genome, via both EWS::FLI1-DNA interactions and multivalent EWS LCD self-interactions (Boulay et al, 2017; Chong et al, 2018; Johnson et al, 2017a). The weak and transient multivalent interactions stabilize EWS::FLI1 binding to GGAA microsatellites, help recruit Pol II to EWS::FLI1 hubs, and are required for EWS::FLI1 to activate transcription of GGAA-affiliated genes and to drive oncogenic transformation (Boulay et al, 2017; Chong et al, 2018; Zuo et al, 2021). Although abolishing or weakening EWS LCD self-interactions is known to disrupt EWS::FLI1-driven transcription of GGAA-affiliated genes, it is unknown how increasing such interactions might impact transcription of these genes.

We tackled this question in patient-derived cells by expressing an exogenous LCD that specifically interacts with endogenous EWS LCD, which is locally concentrated at endogenous EWS::FLI1 hubs. This strategy should lead to an increase in local LCD accumulation at EWS::FLI1 hubs and therefore GGAA-affiliated genes via multivalent LCD-LCD interactions. Specifically, we exploited a knockin Ewing sarcoma cell line A673 that we

recently generated by CRISPR-mediated genome editing. The endogenously expressed EWS::FLI1 is fused to a HaloTag, which can covalently bind to a fluorescent ligand and enable imaging of EWS::FLI1 at native expression levels (Chong et al, 2018). We transiently expressed EWS LCD tagged with mNeonGreen (mNG) and simultaneously imaged EWS::FLI1-Halo and mNG-EWS in live cells with Airyscan confocal super-resolution microscopy. Consistent with the previous report (Chong et al, 2018), we observed that endogenous EWS::FLI1-Halo was distributed as numerous small local high-concentration hubs in the cell nucleus (Figure 1A). This suggests that exogenous EWS LCDs do not noticeably disrupt EWS::FLI1 binding to GGAA microsatellites. Taking advantage of the highly variable levels of transiently expressed mNG-EWS in single cells, we measured the correlation between EWS::FLI1-Halo and mNG-EWS expression levels. Expression of endogenous EWS::FLI1 significantly increased in the presence of high mNG-EWS levels, as measured by both microscopy and flow cytometry (Figures S1A and S1B), though the underlying mechanism is unclear. This result suggests an increased availability of EWS::FLI1 to form hubs with exogenous EWS expression. On the other hand, mNG-EWS distributed throughout the cell nucleus with some minor heterogeneity, but no detectable formation of large, discrete, and droplet-like puncta often attributed to LLPS (Figure 1A). We detected enrichment of exogenous EWS LCDs at many individual EWS::FLI1 hubs (Figure 1A) and clearly demonstrated such enrichment by averaging the images of >500 hubs (Figure 1B). By plotting the averaged radial intensity profiles of both EWS::FLI1 and EWS LCDs surrounding the center of EWS::FLI1 hubs, we confirmed that the maximum concentration of exogenous EWS LCDs locates at the hub center (Figure 1B). These results together suggest an increase of total local EWS LCD concentrations and EWS LCD self-interactions in endogenous EWS::FLI1 hubs upon exogenous EWS LCD expression.

To examine the effect of increasing EWS LCD self-interactions on EWS::FLI1-driven transcription, we performed simultaneous confocal imaging of transiently expressed mNG-EWS, endogenous EWS::FLI1-Halo, and intron RNA fluorescence *in situ* hybridization (FISH) targeting genes adjacent to GGAA microsatellites activated by EWS::FLI1, including *ABHD6* and *CAV1* (Gangwal et al, 2008; Guillon et al, 2009) (Figure 1C). Intron RNA FISH

Figure 1. Overexpressed EWS LCD accumulates at endogenous EWS::FLI1 hubs and represses EWS::FLI1-driven transcription

(A) Airyscan confocal super-resolution images of knockin A673 cells expressing endogenous EWS::FLI1-Halo (JF646 labeled) in the absence or presence of exogenous mNG-EWS expression. The region surrounding one particular EWS::FLI1 hub is zoomed in. mNG-EWS enrichment at the hub is visible but buried in high background.

(B) (Upper) Averaged mNG-EWS image at 539 EWS::FLI1 hubs from three cells. (Lower) Radial intensity profiles of mNG-EWS (blue) and EWS::FLI1-Halo (orange) surrounding the center of EWS::FLI1 hubs on the averaged image.

(C) Confocal fluorescence images of transiently expressed mNG-EWS, endogenous EWS::FLI1-Halo (JFX549 labeled), intron RNA FISH targeting *ABHD6* gene (Quasar 670 labeled, yellow), and DNA (Hoechst labeled, blue) in the knockin A673 cells. The two cells zoomed in show that the level of *ABHD6* transcription negatively correlates with the level of mNG-EWS expression.

(D–F) Boxplots of intron RNA FISH intensities of *ABHD6* (D), *CAV1* (E), or *GAPDH* (F) genes after all the gene loci are categorized based on the corresponding nuclear mNG-EWS intensity. The x axis lists the order of magnitude of mNG intensities in each category. Individual gene loci are plotted in gray. *: statistically significant decrease in the RNA FISH intensity of specific mNG-positive categories compared with the mNG-negative category ($p < 0.05$, two-sample t test). NS, non-significant difference between two categories.

(G) (Upper) Averaged fluorescence intensities of intron RNA FISH (blue) and mNG-EWS (orange) at the *ABHD6* gene loci within each category. *: statistically significant increase in the mNG intensities of low-percentile *ABHD6* gene loci based on the RNA FISH intensity compared with high-percentile loci ($p < 0.05$, two-sample t test). Error bars represent bootstrapped standard deviation. (Bottom) Averaged intron RNA FISH images of *ABHD6* gene loci in four categories based on the percentile rank of intron RNA FISH intensity. Each image is averaged from 211 gene loci.

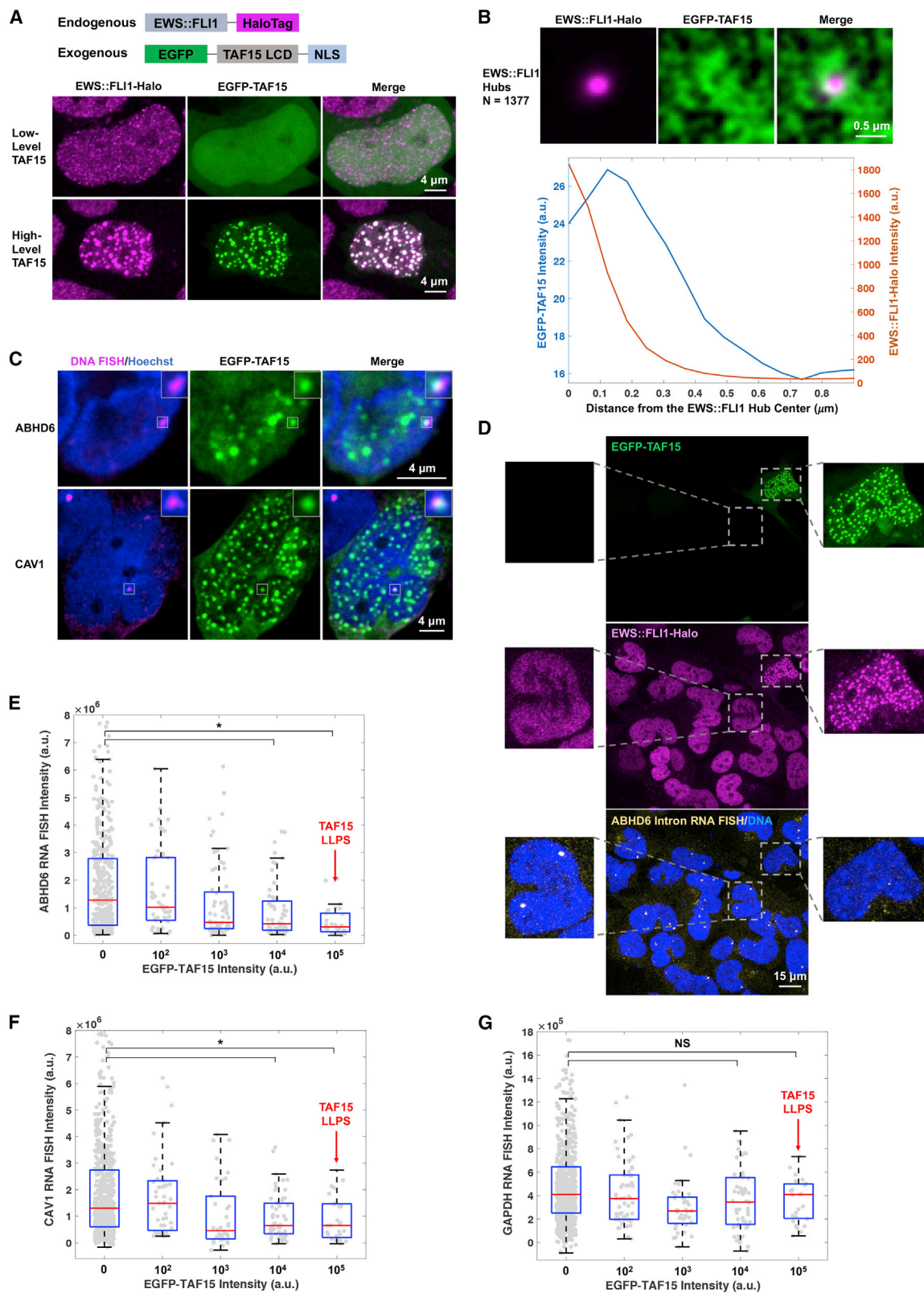
labels RNA at gene loci that are being actively transcribed, and the fluorescence intensity of a FISH punctum is proportional to the number of nascent transcripts produced from the gene locus. We quantified the RNA FISH intensity of each gene locus and categorized all the loci based on the corresponding nuclear mNG-EWS intensity. Boxplots of the categories showed that transcription of *ABHD6* and *CAV1* significantly decreased with an increase in EWS LCD expression (Figures 1D and 1E). As a control, no decrease of endogenous gene transcription was seen upon expression of mNG alone (Figures S1C–S1E). Moreover, transcription of *GAPDH*, a control gene not regulated by EWS::FLI1, remained unaltered regardless of EWS LCD expression (Figure 1F). To further demonstrate the relationship between EWS LCD expression and the transcription of GGAA-affiliated genes, we ranked all *ABHD6* gene loci based on their RNA FISH intensities, sorted them into four percentile-based categories, and averaged the fluorescence intensities of both the RNA FISH and mNG-EWS of all the loci within each category. Across decreasing quartiles of *ABHD6* RNA FISH intensity, the average mNG-EWS intensity significantly increased (Figure 1G), confirming that transcription of *ABHD6* decreases with increasing local EWS LCD concentration. We observed a similar inverse correlation between EWS LCD expression and transcription of another GGAA-affiliated gene *CAV1*, but not the control gene *GAPDH* (Figures S1F and S1G). We note that although endogenous EWS::FLI1 expression varies in single cells, which by itself results in a variable local EWS LCD concentration at GGAA-affiliated genes, we detected no correlation between *ABHD6* or *CAV1* RNA FISH intensity and the nuclear intensity of endogenous EWS::FLI1-Halo in cells without exogenous EWS LCD expression (data not shown). This is due to a high variation of intron RNA FISH intensities stemming from the intrinsic stochasticity of gene transcription and a narrow dynamic range of endogenous EWS::FLI1 levels. Even if variable endogenous EWS::FLI1 expression in single cells does cause a difference in transcription of *ABHD6* or *CAV1*, such small differences would be buried in the intrinsic high variation of RNA FISH intensities and be hard to detect. Yet, our approach of expressing exogenous EWS LCDs to significantly increase local EWS LCD concentrations allowed us to detect effects on target gene transcription.

We observed some local high-concentration regions of exogenous EWS LCDs not colocalizing with EWS::FLI1 hubs, consistent with interactions between the EWS LCD and proteins other than EWS::FLI1 (Figure 1A). Thus, one possibility is that EWS LCDs accumulating at intracellular locations other than EWS::FLI1 hubs compete off EWS::FLI1 from GGAA-affiliated genes via EWS LCD self-interactions. This behavior would also lead to an inverse correlation between exogenous EWS LCD expression and EWS::FLI1-driven transcription that we have observed. To test this possibility, we quantified the integrated EWS::FLI1-Halo intensity at each *ABHD6* and *CAV1* gene locus and plotted the intensity against the corresponding nuclear mNG-EWS intensity. We found the local EWS::FLI1-Halo intensity at both *ABHD6* and *CAV1* loci significantly increased with EWS LCD expression (Figures S1H and S1I), which is inconsistent with the above competition hypothesis but confirms an increase in total local EWS LCD concentration at GGAA-affiliated genes.

Together, our results suggest that exogenous EWS LCD expression leads to enhanced EWS LCD self-interactions at GGAA-affiliated genes and specifically represses endogenous EWS::FLI1-driven transcription. Combining this finding with previous reports that EWS LCD self-interactions are required for EWS::FLI1 to activate transcription (Boulay et al, 2017; Chong et al, 2018), we conclude that transactivation by EWS::FLI1 requires a tightly regulated amount of EWS LCD self-interactions at endogenous target genes, whereby either decreasing or increasing these interactions compromises transcriptional output. The small, transient endogenous EWS::FLI1 hubs we observed previously under native conditions achieved an optimal amount of productive LCD-LCD interactions. Here, we have shown that unbalancing the system beyond this sweet spot reduces target gene expression, shedding light on the fragile stoichiometry of the system. Alternatively, however, it could be that we failed to achieve enhanced transcription because we never reached levels of LCD-LCD interactions that promoted LLPS, as has been proposed by recent reports (Schneider et al, 2021; Wei et al, 2020).

TAF15 LCD binding to EWS::FLI1 hubs induces large LLPS-like puncta and severely represses EWS::FLI1-driven transcription

We next investigated how a more potently phase-separating LCD from TAF15, which efficiently interacts with EWS LCD (Chong et al, 2018), might impact the LLPS behaviors and functions of EWS::FLI1. TAF15 LCD is known to function as a potent transactivation domain and multivalently interact with intrinsically disordered regions in essential components of the transcription machinery, e.g., Pol II (Chong et al, 2018; Kwon et al, 2013; Wei et al, 2020). Moreover, TAF15 LCD was recently reported to amplify transcription in cells upon LLPS (Wei et al, 2020). We simultaneously imaged transiently expressed TAF15 LCD tagged with EGFP and endogenous EWS::FLI1-Halo in the knockin A673 cells (Figure 2A). Whereas EGFP-TAF15 distributes throughout the cell nucleus at low expression levels, it forms discrete and prominent droplet-like puncta at high expression levels, a likely though not definitive sign of LLPS (McSwigen et al, 2019b). Although endogenous EWS::FLI1-Halo still forms numerous small hubs in the presence of low levels of EGFP-TAF15, its distribution changes significantly upon apparent LLPS and becomes strongly enriched in TAF15 LCD puncta, leaving the much smaller endogenous EWS::FLI1 hubs depleted (Figure 2A). This result is consistent with our previous study showing heterotypic but selective interactions between TAF15 LCDs and EWS LCDs. We also detected such interactions at EWS::FLI1 hubs when EGFP-TAF15 is expressed at low levels by averaging the images of >1,300 hubs (Figure 2B). We found that TAF15 LCD is more enriched at the periphery than the center of EWS::FLI1 hubs, as was observed with EWS LCDs, potentially due to differences in the affinity of heterotypic interactions compared with that of homotypic interactions (Chong et al, 2018). Nevertheless, this result confirms that at low expression levels, TAF15 LCDs binds to endogenous EWS::FLI1 hubs. Exogenous expression of TAF15 LCDs did not reduce the expression of endogenous EWS::FLI1. Instead, flow cytometry showed no correlation between TAF15 LCD



(legend on next page)

and EWS::FLI1 expression, and microscopy revealed a slight increase of EWS::FLI1 expression at TAF15 LCD levels high enough to form puncta (Figures S2A and S2B). Thus, exogenous TAF15 LCDs, when expressed at low levels insufficient to induce LLPS, increase total local LCD concentrations and therefore multivalent LCD-LCD interactions in endogenous EWS::FLI1 hubs formed at GGAA microsatellites.

In order to examine the spatial relationship between TAF15 LCD puncta and GGAA-affiliated genes in cells with putative LLPS, we simultaneously imaged highly expressed EGFP-TAF15 and 3D DNA FISH targeting two such genes (*ABHD6* or *CAV1*). We found in cells with TAF15 LLPS, 29.7% of the 37 detected *ABHD6* loci and 28.2% of the 39 detected *CAV1* loci colocalize with TAF15 LCD puncta (Figure 2C). *ABHD6* or *CAV1* gene-associated TAF15 LCD puncta are often slightly off-center from the gene loci, consistent with our findings in low-TAF15 cells (Figure 2B). Our observation that not all detected GGAA target gene loci are associated with TAF15 LCD puncta naturally results from the fact that there are, at most, a few hundred TAF15 LCD puncta per cell nucleus, which is orders of magnitude fewer than the ~6,000 EWS::FLI1-bound GGAA microsatellites across the human genome (Johnson et al, 2017b). Such number mismatch results in a dramatically unbalanced distribution of TAF15 LCD puncta as well as puncta-binding, endogenously expressed transcription regulators, e.g., EWS::FLI1, among all GGAA-affiliated gene loci in a cell. Whereas some of the loci are associated with puncta, having increased LCD-LCD interactions and enriching endogenous EWS::FLI1, the remaining loci are starved of TAF15 LCDs as well as EWS::FLI1, which would otherwise form hubs more efficiently at the loci under native conditions.

We next examined how exogenous expression of TAF15 LCD affects EWS::FLI1-driven transcription of GGAA-affiliated genes with intron RNA FISH (Figure 2D) as described above for EWS LCDs. Boxplots showed that the transcription of *ABHD6* and *CAV1* markedly decreased when TAF15 LCD expression increased. The occurrence of apparent LLPS did not reverse this trend. In fact, maximal inhibition of transactivation coincided with concentrations of exogenous TAF15 LCD required to form the prominent droplet-like puncta (Figures 2E and 2F). As controls, expression of EGFP alone in these cells at comparable levels had no effect on transcription of *ABHD6* (Figures S2C–S2E), and transcription of a control gene, *GAPDH*, also did not track with TAF15 LCD expression (Figure 2G), suggesting that the effect of TAF15

LCD expression on endogenous transcription is specific to GGAA-affiliated EWS::FLI1 target genes. By simultaneously imaging endogenous EWS::FLI1-Halo and gene loci (Figure 2D), we also examined the possibility that exogenous TAF15 LCDs accumulated outside EWS::FLI1 hubs would compete off EWS::FLI1 from GGAA-affiliated genes and therefore decrease their transcription. We quantified the integrated EWS::FLI1-Halo intensity at each *ABHD6* and *CAV1* gene locus and plotted the intensity against the corresponding nuclear EGFP-TAF15 intensity. We found that the local EWS::FLI1-Halo intensity slightly increased at *ABHD6* loci and remained constant at *CAV1* loci when the TAF15 LCD is highly expressed (Figures S2F and S2G). This result argues against the above possibility and further confirms an increase of total local LCD concentrations at GGAA-affiliated genes upon exogenous TAF15 LCD expression.

Taken together, these results suggest that allowing exogenous TAF15 LCDs to accumulate at endogenous EWS::FLI1 hubs at GGAA-affiliated genes represses EWS::FLI1-driven transcription even after occurrence of TAF15-induced LLPS. Similar to increasing EWS LCD self-interactions, increasing heterotypic TAF15-EWS LCD interactions at endogenous EWS::FLI1 target genes also unbalances the sweet spot of LCD-LCD interactions needed to drive transactivation (Boulay et al, 2017; Chong et al, 2018). Notably, our results are not consistent with the model in which transactivation depends on the formation of LLPS condensates at target genes (Boija et al, 2018; Cho et al, 2018; Hnisz et al, 2017; Sabari et al, 2018; Schneider et al, 2021; Wei et al, 2020). Whereas the mechanism by which forced LLPS inhibits transcription of specific endogenous genes remains unclear, one possibility is that when TAF15 LCD puncta are formed at locations other than these gene loci, the relatively stable and transcriptionally nonproductive puncta trap EWS::FLI1, effectively reducing the functional pool of EWS::FLI1 molecules that can freely access the target genes and trigger transactivation. Because some GGAA-affiliated gene loci are associated with TAF15 LCD puncta, it is not feasible to evaluate the trapping mechanism in this experimental setup.

Ectopic nucleolar EWS LCD self-interactions sequester endogenous EWS::FLI1 to the nucleolus and repress EWS::FLI1-driven transcription and oncogenic transformation

We next tested the aforementioned trapping mechanism in a series of experiments employing targeted mislocalization of TFs to

Figure 2. TAF15 LCD overexpression and phase separation repress EWS::FLI1-driven transcription

- (A) Airyscan confocal super-resolution images of endogenous EWS::FLI1-Halo (JF646 labeled) and transiently expressed EGFP-TAF15 in two knockin A673 cells with different levels of EGFP-TAF15.
- (B) (Upper) Averaged EGFP-TAF15 image at 1377 EWS::FLI1 hubs from nine cells without apparent LLPS of TAF15. (Lower) Radial intensity profiles of EGFP-TAF15 (blue) and EWS::FLI1-Halo (orange) surrounding the center of EWS::FLI1 hubs on the averaged image.
- (C) Airyscan confocal super-resolution images of 3D DNA FISH targeting *ABHD6* or *CAV1* genes (enhanced Cy5 labeled, magenta), DNA (Hoechst labeled, blue), and droplet-like puncta of EGFP-TAF15 in two knockin A673 cells. The region surrounding a gene locus in each cell is zoomed in. A TAF15 punctum colocalizes with each of the loci.
- (D) Confocal fluorescence images of transiently expressed EGFP-TAF15, endogenous EWS::FLI1-Halo (JFX549 labeled), intron RNA FISH targeting *ABHD6* gene (Quasar 670 labeled, yellow), and DNA (Hoechst labeled, blue) in the knockin A673 cells. The two cells zoomed in show that the level of *ABHD6* transcription negatively correlates with the level of EGFP-TAF15 expression.
- (E–G) Boxplots of intron RNA FISH intensities of *ABHD6* (F), *CAV1* (G), or *GAPDH* (H) genes after all the gene loci are categorized based on the corresponding nuclear EGFP-TAF15 intensity. The x axis lists the order of magnitude of EGFP intensities in each category. The category with apparent LLPS of TAF15 is pointed with a red arrow on each plot. Individual gene loci are plotted in gray. *: statistically significant decrease in the RNA FISH intensity of specific EGFP-positive categories compared with the EGFP-negative category ($p < 0.05$, two-sample t test). NS, non-significant difference between two categories.

the nucleolus, a membraneless organelle lacking Pol II transcription and one of the best-characterized examples of a subcellular compartment formed by LLPS (Brangwynne et al, 2011; Riback et al, 2020). We took advantage of the fact that the EWS LCD specifically interacts with itself and hypothesized that mislocalizing EWS LCD-LCD interactions to the nucleolus could lead to the co-recruitment of endogenous EWS::FLI1, mimicking the scenario where TAF15 LCD puncta trap endogenous EWS::FLI1. Specifically, we transiently expressed in the knockin A673 cells and mNG-tagged EWS LCD fused to a nucleolar protein, NPM1 (Mitrea et al, 2016, 2018), and simultaneously imaged EWS::FLI1-Halo and mNG-EWS-NPM1 in live cells (Figure 3A). We found mNG-EWS-NPM1 mostly localizes to the nucleolus, as expected. Interestingly, endogenous EWS::FLI1-Halo that normally localizes to the nucleoplasm is now recruited to the nucleolus. The nucleolar enrichment of EWS::FLI1-Halo, calculated as the ratio of its nucleolar to nucleoplasmic concentration ($[\text{EWS::FLI1}]_{\text{nucleolus}}/[\text{EWS::FLI1}]_{\text{nucleoplasm}}$), increases with the expression level of mNG-EWS-NPM1 (Figures S3A and S3B). In contrast, EWS::FLI1-Halo remains in the nucleoplasm in cells that express a control mNG-tagged NPM1 alone (Figures 3A and S3B). These results suggest that the observed nucleolar recruitment of EWS::FLI1 by EWS-NPM1 is driven by EWS LCD self-interactions in the nucleolus. Our results here suggest that despite being very transient (Chong et al, 2018), multivalent LCD-LCD interactions *in vivo* can be strong enough to outcompete stoichiometric cognate TF-DNA-binding interactions and trap a TF away from nucleoplasmic chromatin where it normally binds.

We next tested how nucleolar trapping of EWS::FLI1 influences its transactivation of endogenous target genes and associated oncogenic transformation functions. First, we measured EWS::FLI1-driven transcription at the single-cell level. Specifically, we performed simultaneous confocal imaging of transiently expressed mNG-EWS-NPM1, endogenous EWS::FLI1-Halo, and intron RNA FISH targeting GGAA-affiliated genes, *ABHD6* or *CAV1* (Figure 3B). We quantified the RNA FISH intensity of each detected gene locus, categorized all the loci based on nucleolar mNG-EWS-NPM1 intensity or nucleolar EWS::FLI1-Halo enrichment, and then generated boxplots of individual categories (Figures S3C, S3D, and S3F). The boxplots showed that transcription of *ABHD6* and *CAV1* significantly decreased with increasing EWS-NPM1 expression and concomitant enrichment of nucleolar EWS::FLI1 (Figures 3C and 3D). The decrease of endogenous gene transcription is not due to overexpression of NPM1, as expressing mNG-NPM1 did not affect the transcription of *ABHD6* (Figure S3E). Moreover, transcription of the control *GAPDH* gene does not change with EWS-NPM1 expression (Figure S3G) or nucleolar EWS::FLI1 enrichment (Figure 3E), suggesting that the effect of nucleolar trapping of EWS::FLI1 on endogenous transcription is specific to GGAA-affiliated EWS::FLI1 target genes. EWS-NPM1 could potentially be recruited to endogenous EWS::FLI1 hubs via EWS LCD self-interactions and cause repression of EWS::FLI1-driven transcription. We averaged the images of >800 endogenous EWS::FLI1 hubs to test this reverse recruitment possibility but barely detected any enrichment of EWS-NPM1 at the hubs (Figure S3H). This is likely due to the low availability of

both EWS::FLI1 and EWS-NPM1 in the nucleoplasm. This finding is quite distinct from the scenario we observed above (Figure 1B) of exogenous EWS LCD accumulating at EWS::FLI1 hubs. The lack of EWS-NPM1 accumulation at EWS::FLI1 hubs suggests that our detected repression of EWS::FLI1-driven transcription is caused by nucleolar trapping of EWS::FLI1, which effectively lowers the available concentration of EWS::FLI1 in the nucleoplasm and reduces its binding to and activation of target genes.

We next used a series of ensemble assays to investigate how nucleolar trapping of EWS::FLI1 affects its function in driving the oncogenic transcription program in Ewing sarcoma cells. To this end, we engineered the knockin A673 cells to make a clonal cell line that expresses high levels of mNG-EWS-NPM1 upon doxycycline induction ($[\text{EWS::FLI1}]_{\text{nucleolus}}/[\text{EWS::FLI1}]_{\text{nucleoplasm}} \sim 1.85 \pm 0.53$ [standard deviation], measured in 164 randomly chosen cells). As a control, we made a knockin clonal cell line with inducible expression of mNG-NPM1 at levels similar to mNG-EWS-NPM1, as described above (Figure S4A). Comparing these two cell lines provides a useful way to reveal more global functional impacts of nucleolar trapping of EWS::FLI1. First, to examine how nucleolar trapping of EWS::FLI1 affects its transactivation function, we performed reverse transcription quantitative polymerase chain reaction (RT-qPCR) to measure mRNA levels of 22 GGAA-affiliated EWS::FLI1 target genes and four control genes not regulated by EWS::FLI1 (Boulay et al, 2017; Chong et al, 2018) in both cell lines, before and after doxycycline induction. Whereas the control genes are expressed at constant levels regardless of the presence of exogenous EWS-NPM1 or NPM1 (Figure S4B), most GGAA-affiliated genes have transcription levels differentially affected by EWS-NPM1 versus NPM1 (Figure 3F). Out of the 22 GGAA-affiliated genes, 45.5% are expressed significantly lower upon induction of EWS-NPM1 than upon induction of NPM1, 18.2% are expressed significantly higher upon induction of EWS-NPM1 than upon induction of NPM1, and 36.4% are equally affected by EWS-NPM1 and control NPM1. Our result suggests that many more GGAA-affiliated genes have transcription repressed rather than enhanced by nucleolar trapping of EWS::FLI1, confirming the overall repressive effect of the nucleolar trapping on EWS::FLI1-driven transcription. The finding that transcription of some GGAA-affiliated genes is unaffected or even enhanced by nucleolar trapping is likely because optimal levels of productive LCD-LCD interactions are gene specific. One can imagine that reducing the number of EWS::FLI1 molecules at these genes by the nucleolar trapping either pushed the system closer to their optimum or failed to sufficiently unbalance the optimum. Next, we examined how nucleolar trapping of EWS::FLI1 affects cell proliferation by monitoring cell growth over time with the xCELLigence real-time cell analysis system (Witzel et al, 2015). We found that although the knockin A673 cells proliferate after induction of NPM1, they completely stop proliferating 48 h after induction of EWS-NPM1 (Figure S4C). Meanwhile, using soft agar colony formation assay (Lessnick et al., 2002), we found that EWS-NPM1 induction in the knockin A673 cells abolished their malignant transformation phenotype, i.e., growth in soft agar, although this could also be linked to general growth arrest. In contrast, cells after NPM1 induction continue forming colonies in soft agar, albeit with lower efficiency than uninduced cells (Figures 3G and 3H).

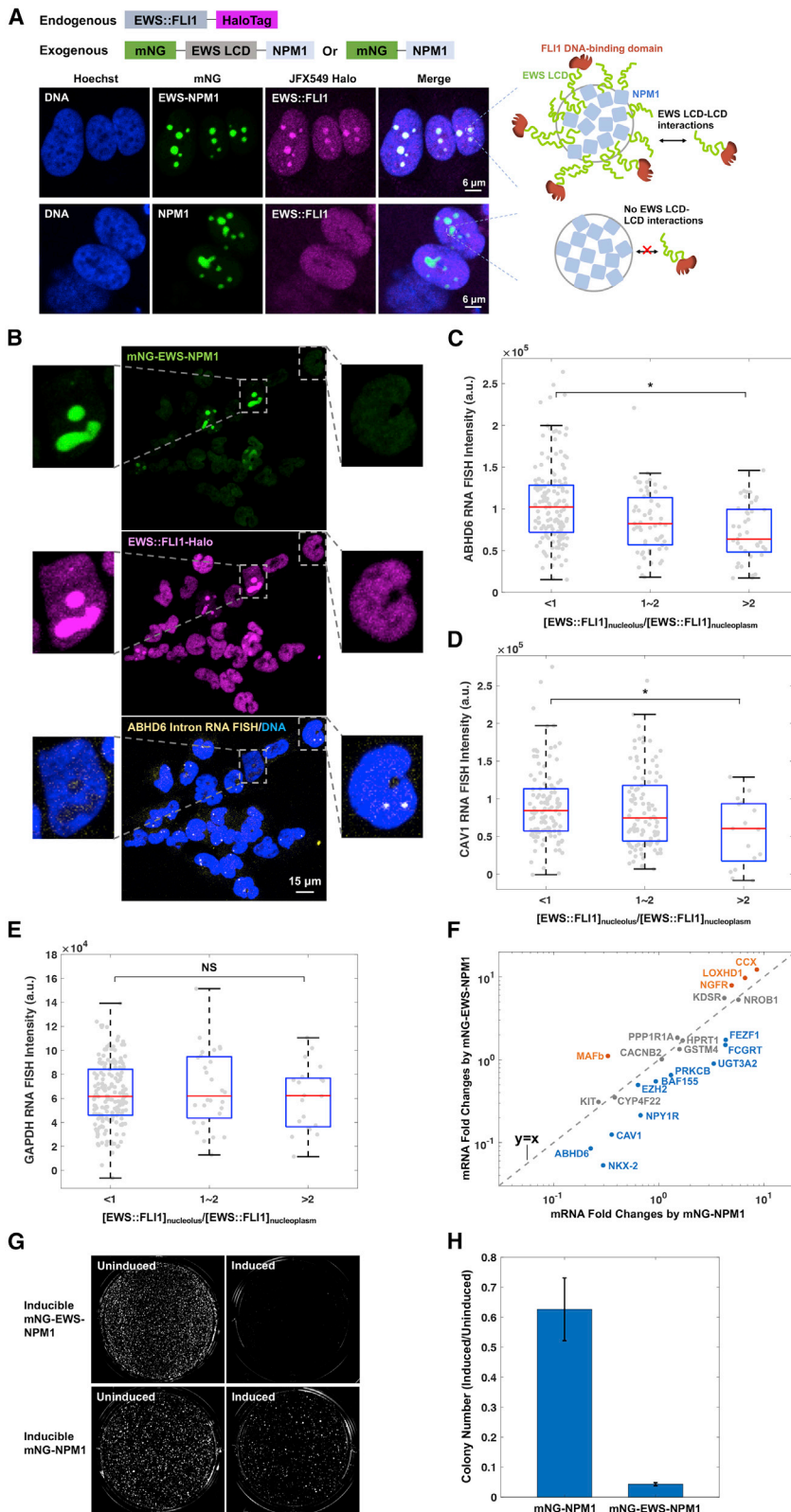


Figure 3. Nucleolar trapping of EWS::FLI1 represses its transcriptional activation and oncogenic transformation functions

(A) (Left) Airyscan confocal super-resolution images of DNA (Hoechst labeled), transiently expressed mNG-EWS-NPM1 or mNG-NPM1, and endogenous EWS::FLI1-Halo (JFX549 labeled) in the knockin A673 cells. (Right) Schematics for protein-protein interactions within the nucleolus.

(B) Confocal fluorescence images of transiently expressed mNG-EWS-NPM1, endogenous EWS::FLI1-Halo (JFX549 labeled), intron RNA FISH targeting *ABHD6* gene (Quasar 670 labeled, yellow), and DNA (Hoechst labeled, blue) in the knockin A673 cells. The two cells zoomed in show that the level of *ABHD6* transcription negatively correlates with the level of mNG-EWS-NPM1 expression.

(C–E) Boxplots of intron RNA FISH intensities of *ABHD6* (C), *CAV1* (D), or *GAPDH* (E) genes after all the gene loci are categorized based on the nucleolar enrichment of EWS::FLI1 in corresponding cells. The x axis lists the range of $[EWS::FLI1]_{nucleolus}/[EWS::FLI1]_{nucleoplasm}$ ratios for each category. Individual gene loci are plotted in gray. *: statistically significant decrease in the RNA FISH intensity of cells with nucleolar enrichment of EWS::FLI1 compared with cells without nucleolar enrichment of EWS::FLI1 ($p < 0.05$, two-sample t test). NS, non-significant difference between two categories.

(F) mRNA fold changes of 22 GGAA-affiliated EWS::FLI1 target genes by induction of mNG-EWS-NPM1 (y coordinate) versus induction of mNG-NPM1 (x coordinate) as measured by RT-qPCR. For each target gene, the mRNA level in induced cells was first normalized using the average of four invariant genes (Figure S4B) and then calculated as a fold change relative to the normalized mRNA level in uninduced cells. On the 2D graph, genes expressed lower upon induction of EWS-NPM1 than upon induction of NPM1 and vice versa are separated by the function plot $y = x$. Genes having $y < x$ with statistical significance are plotted in blue, genes having $y > x$ with statistical significance are plotted in orange, and genes without statistically significant difference between y and x values are plotted in gray ($p < 0.05$, two-sample t test).

(G) Soft agar colony formation assays for the knockin A673 cells with inducible expression of mNG-EWS-NPM1 or mNG-NPM1.

(H) Fold change of the number of colonies (diameter $> 220 \mu m$) in soft agar by induction of mNG-EWS-NPM1 or mNG-NPM1, quantified from (G). Error bars represent standard errors.

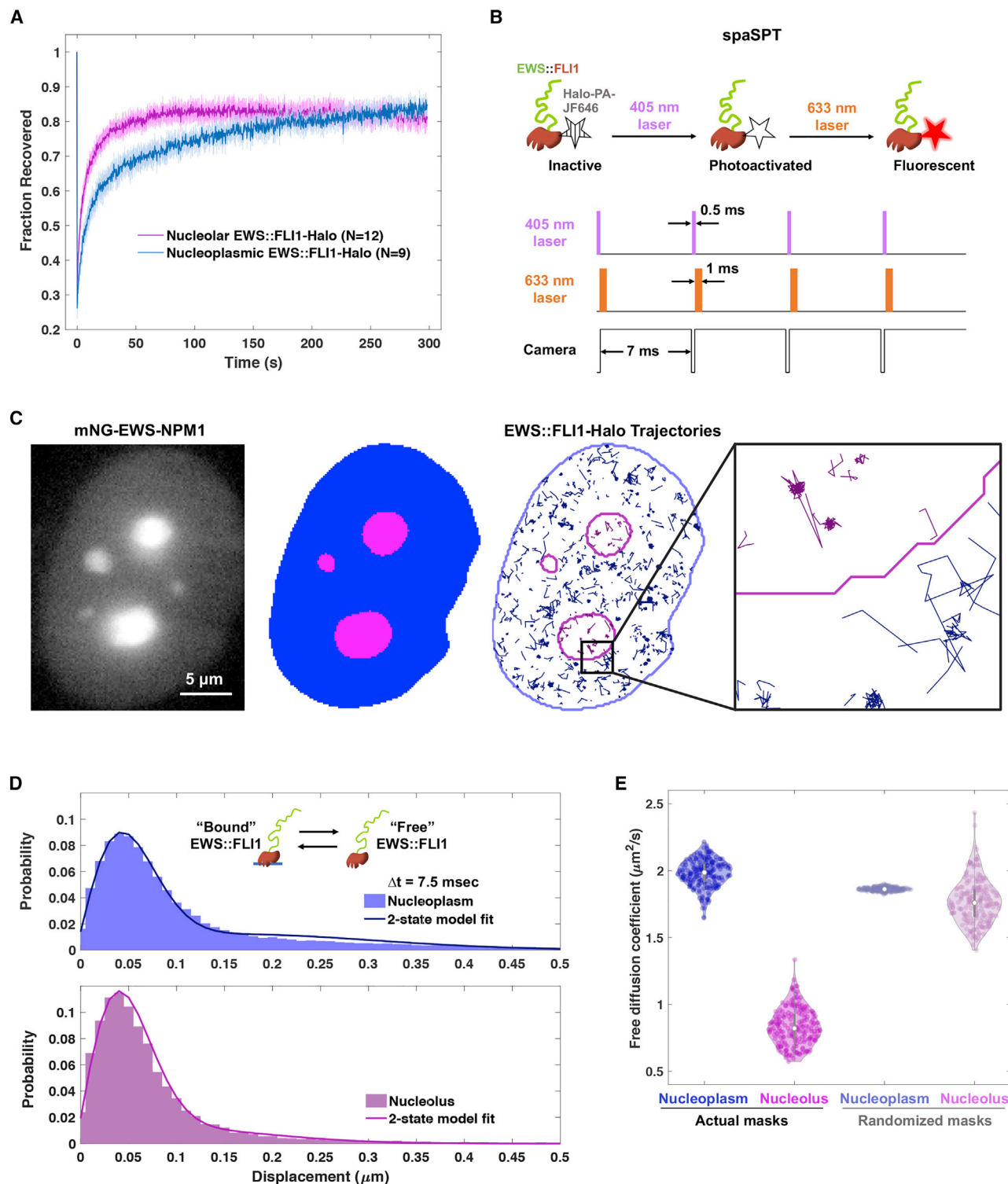


Figure 4. EWS::FLI1 changes its dynamic behaviors when recruited to the nucleolus

(A) Averaged FRAP curve of endogenous EWS::FLI1-Halo in the nucleoplasm (blue) or nucleolus (magenta). Error bars represent standard deviations. (B) Schematic of stroboscopic photo-activatable single-particle tracking (spaSPT). Living knockin A673 cells with endogenous EWS::FLI1-Halo expression are stained with photo-activatable HaloTag ligand, PA-JF646. Short pulses of 405- and 633-nm lasers are used, respectively, to activate and excite PA-JF646 dye to achieve ms temporal resolution and differentiate “free” molecules and “bound” molecules.

(legend continued on next page)

These results together suggest that nucleolar trapping of EWS::FLI1 represses the oncogenic transcription program driven by EWS::FLI1 and strongly inhibits proliferation and malignant transformation of Ewing sarcoma cells. Notably, the ability to tune the subcellular localization of LCD-LCD interactions, thereby sequestering EWS::FLI1 and disrupting its oncogenic functions, suggests a potential new therapeutic strategy for Ewing sarcoma, a devastating cancer still lacking effective molecular therapy.

EWS::FLI1 diffuses more slowly in the nucleolus than in the nucleoplasm

We further investigated how nucleolar trapping of EWS::FLI1 changes its dynamic behavior. Since the nucleolus is well characterized as a LLPS condensate (Brangwynne et al, 2011; Riback et al, 2020), measuring dynamics of EWS::FLI1 in this context provides a unique opportunity to probe how LLPS affects the dynamic behavior of a protein that localizes within condensates. We first measured the fluorescence recovery after photobleaching (FRAP) dynamics of EWS::FLI1 in the nucleolus and in the nucleoplasm, respectively. We found that the FRAP dynamics of nucleolar EWS::FLI1 are significantly different from nucleoplasmic EWS::FLI1 (Figure 4A). Since the FRAP dynamics reflected a mixture of diffusion and molecular interaction dynamics (STAR Methods), accurate quantification of either from FRAP curves was challenging (Sprague et al, 2004). Thus, in order to directly compare the diffusion dynamics of nucleolar and nucleoplasmic EWS::FLI1, we visualized and tracked both immobile and freely diffusing molecules using stroboscopic photo-activatable single-particle tracking (spaSPT) (Elf et al, 2007; Hansen et al, 2017, 2018) (Figure 4B). We expressed mNG-EWS-NPM1 in the knockin A673 cells and performed spaSPT on endogenous EWS::FLI1-Halo labeled with photo-activatable Janelia Fluor 646 (PA-JF646) HaloTag ligand (Grimm et al, 2016). Single-molecule trajectories were classified as either nucleoplasmic or nucleolar, based on binary masks generated using images of mNG-EWS-NPM1 (Figure 4C). Nucleolar and nucleoplasmic trajectories were then separately analyzed using the Spot-On algorithm (Hansen et al, 2018), which fits histograms of single-particle displacements to a two-state model, where EWS::FLI1 can either be freely diffusing (“free”) or immobile and presumably bound to protein or DNA partners (“bound”) (Figure 4D). Spot-On analysis yields the estimates of the fraction of “bound” and “free” molecules as well as the apparent diffusion coefficient for each sub-population (Hansen et al, 2018). Interestingly, the fitted diffusion coefficient of the free sub-population was $1.97 \pm 0.20 \mu\text{m}^2/\text{s}$ (95% bootstrap confidence interval) outside of the nucleoli but only $0.82 \pm 0.26 \mu\text{m}^2/\text{s}$ inside the nucleoli, indicating that EWS::FLI1 diffuses significantly more

slowly in the nucleolus than in the nucleoplasm (Figure 4E). This difference in free diffusion coefficient was much greater than that observed when trajectories were classified using mock nucleolar masks at randomized positions (Figures 4E and S5A), indicating that it does not result merely from geometric biases in trajectory classification. The other fit parameters from Spot-On did not differ significantly from randomized mask controls (Figures S5B and S5C). Taken together, our results are consistent with the model that the nucleolus is a true LLPS compartment displaying properties distinct from the rest of the nucleus, i.e., higher viscosity (Brangwynne et al, 2011; Xiang et al, 2020). As with endogenous nucleolar proteins (Heckert et al, 2021), diffusion of “guest” EWS::FLI1 molecules is reduced when they are recruited to this high-viscosity compartment by EWS-NPM1.

DISCUSSION

Sequence-specific DNA-binding TFs have been established as key regulators of eukaryotic transcription since the early 1980s (Dyana and Tjian, 1983), but how their LCDs execute transactivation has remained mysterious. Recent live-cell single-molecule imaging experiments have revealed that weak, multivalent, but selective interactions occur between LCDs, which drive the formation of highly transient, small, local high-concentration TF hubs at target genomic loci and play an essential role in transactivation. Typically containing <100 molecules with protein-binding dwell times of ~1–2 min, such hubs appear to be distinct from LLPS condensates (Chong et al, 2018), although excessive multivalent LCD-LCD interactions can induce putative LLPS under non-physiological conditions (Bracha et al, 2019; Shin et al, 2017, 2019). Whereas LLPS has been proposed to underlie many cellular functions, including transcription (Banani et al, 2017; Boeynaems et al, 2018; Chong and Mir, 2021; Narlikar et al, 2021; Shin and Brangwynne, 2017), studies that directly link LCD-LCD interactions, LLPS, and transcriptional output are scarce (Schneider et al, 2021; Trojanowski et al, 2021; Wei et al, 2020), and the few existing studies have generated contradictory findings. The fact that rigorous characterization of LLPS *in vivo* has been challenging and often assumed rather than experimentally confirmed (McSwiggen et al, 2019b) adds to the confusion of recent findings. Importantly, no existing study measured the transcription of specific endogenous genes upon manipulation of LCD-LCD interactions or upon induction of LLPS which, in our opinion, would be essential for understanding LCD-interaction-mediated transcription *in vivo* under physiologically relevant contexts.

To fill in these knowledge gaps, here, we measured transcription of a select set of endogenous target genes activated by the

(C) Classification of nucleoplasmic and nucleolar single-particle trajectories acquired in a spaSPT experiment. (Left) Image of mNG-EWS-NPM1 used for segmentation. Pixel intensities are displayed on a logarithmic scale between 3 and 30,000 counts. (Middle) Binary mask showing segmentation of nucleoplasm (blue) and nucleoli (magenta). (Right) Overlay of classified single-particle trajectories (thinner lines) and mask boundaries (thicker lines). Nucleoplasmic trajectories are in blue and nucleolar trajectories are in magenta. Inset: zoom-in of a 2.6- μm square region at the boundary of a nucleolus.

(D) Distribution histograms of displacements in a single 7.5-ms time step for trajectories in the nucleoplasm (upper, blue) and nucleolus (lower, magenta). Each histogram is fit with a two-state model. Inset shows depiction of the two-state model where EWS::FLI1 can either be freely diffusing or bound to protein or DNA partners.

(E) Fitted diffusion coefficient of freely diffusing molecules in the nucleoplasm (blue) and nucleolus (magenta). Left two columns: fits for trajectories classified using actual nucleolar masks. Violin plots show the distribution of 200 bootstrap replicates resampled by cell with replacement. Right two columns: fits for trajectories classified using 200 distinct sets of randomized nucleolar masks (see STAR Methods).

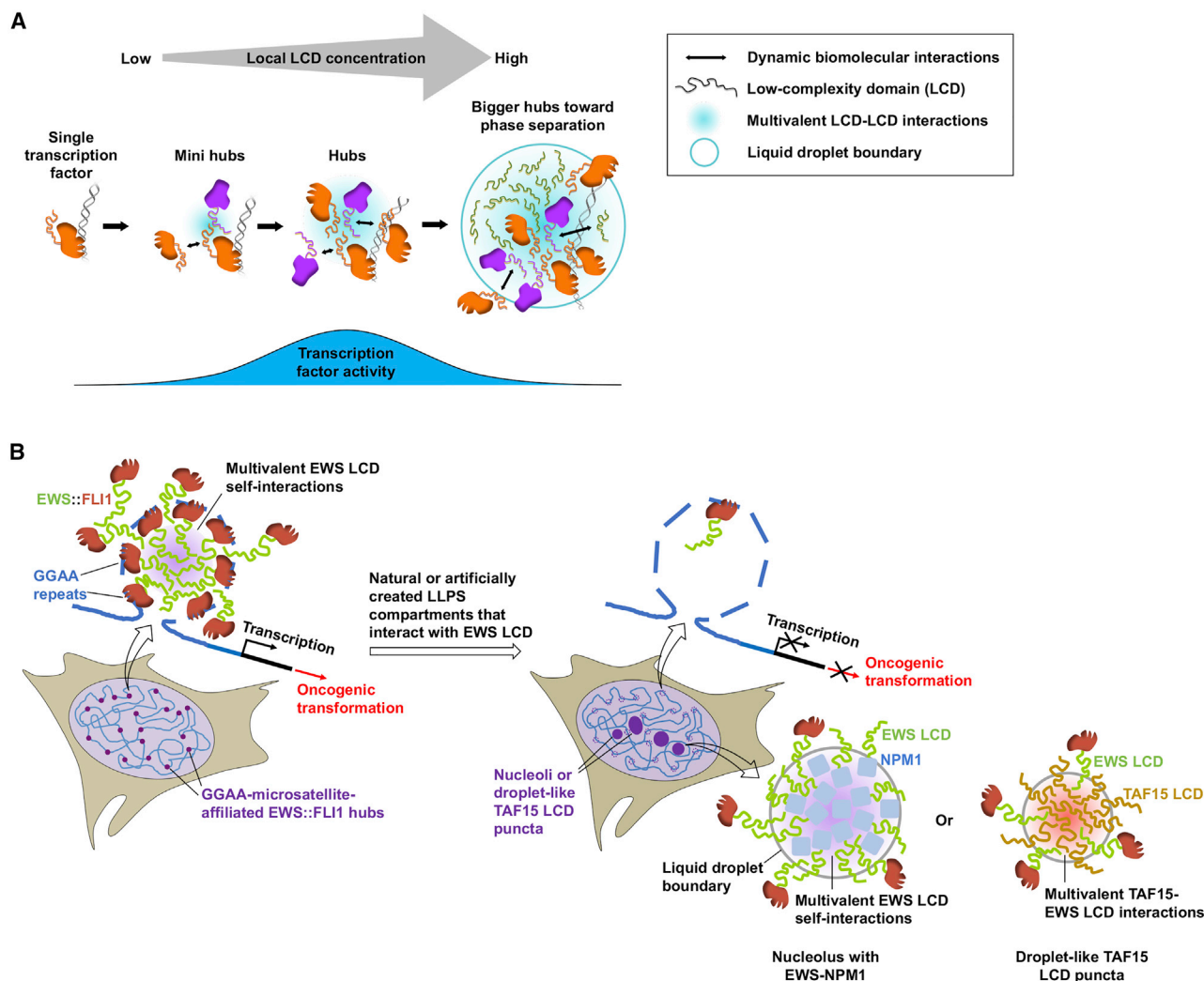


Figure 5. Models for LCD-interaction-mediated transcription

(A) Goldilocks principle of transcriptional activation: effective gene activation requires an optimal amount of multivalent LCD-LCD interactions. Overly high amounts of LCD-LCD interactions and LLPS at target genes repress transcription.

(B) LLPS compartments formed away from EWS::FLI1 target genes trap endogenous EWS::FLI1 within the compartments via homotypic or heterotypic LCD-LCD interactions, causing repression of EWS::FLI1-driven oncogenic transcription.

oncogenic TF EWS::FLI1 upon tuning the amount and localization of its LCD-LCD interactions in patient-derived cells. In the first part of this work, we employed quantitative single-cell imaging to study how increasing either homotypic or heterotypic LCD-LCD interactions at EWS::FLI1 target genes associated with GGAA microsatellites affects transcription of the genes. Our findings indicate that the transactivation activity of EWS::FLI1 does not monotonically increase with the amount of local LCD-LCD interactions at select target genes and instead reaches an optimum with the endogenous amount of interactions and that further increases in LCD-LCD interactions can lead to apparent LLPS that invariably causes repression of endogenous gene transcription (Figure 5A). This “Goldilocks principle” underlying EWS::FLI1-driven transcription—where “just the right amount” of LCD-LCD interactions is required for

efficient gene activation—may be general to mammalian transcription and applicable to many other TFs, though the optimal amount of LCD-LCD interactions likely varies with specific TFs and target genes. Intriguingly, we observed potent transcriptional repression of endogenous cognate genes upon apparent LLPS driven by TAF15 LCD, in contrast to the previously reported increase in overall cellular transcription upon light-induced TAF15 LLPS (Wei et al, 2020). We do not yet have sufficient data to provide any firm mechanistic explanation for this apparent disparity, but one possibility is related to the ability of LLPS to redistribute TFs and components of the transcription machinery among genes via heterotypic LCD-LCD interactions (Figures 2A and 5B). Whereas LLPS unbalances the “Goldilocks optimum” for one set of genes, it may simultaneously tune the local concentrations of transcription regulators toward the

optimum for other genes. Thus, it may not be entirely unexpected to find that overall transcription is increased while specific target genes are repressed upon LLPS. It will be important in the future to investigate how increasing levels of LCD-LCD interactions toward LLPS affects the global transcriptome of a cell. Another key endeavor will be to decipher the molecular basis for the repressive effects of excessive LCD-LCD interactions on transcription, even in the absence of LLPS. Moreover, the quantitative single-cell imaging methods we developed to investigate EWS::FLI1 could pave the way to test the Goldilocks principle for other TFs in future studies.

In the second part of this work, we demonstrated that multivalent EWS LCD self-interactions artificially created in the nucleolus are strong enough to relocate EWS::FLI1 from chromatin to the nucleolus, repress EWS::FLI1-driven transcription, and inhibit malignant transformation of Ewing sarcoma cells (Figure 5B). Our findings reveal an important property of EWS LCD self-interactions; i.e., when recruited into the nucleolus, they can overcome EWS::FLI1-DNA-binding interactions and effectively sequester TFs in a non-productive compartment. We expect similar strategies may allow trapping of EWS::FLI1 in other ectopic subcellular locations as well. The ability of subcellular mislocalization of LCD-LCD interactions to disrupt EWS::FLI1-chromatin binding and transactivation suggests a potentially new therapeutic strategy for Ewing sarcoma. If the EWS-NPM1 protein we used could be replaced by smaller and more deliverable drug-like molecules that can specifically interact with the EWS LCD and can be localized to an ectopic subcellular structure, one could imagine using such molecules to sequester EWS::FLI1 to the subcellular structure to disrupt its function. Notably, small molecule trabectedin and its analog are reported to sequester EWS::FLI1 to the nucleolus and disrupt its functions (Harlow et al, 2016). Although this sequestration is through a mechanism other than mislocalized LCD-LCD interactions, it shows the feasibility of a sequestration-based therapeutic strategy. Similar approaches based on mislocalizing LCD-LCD interactions could potentially be used to target many other disease-causing TFs that remain notoriously difficult targets for developing drugs.

Our work on nucleolar targeting additionally sheds light on methods to more rigorously diagnose LLPS *in vivo*. Differential molecular diffusion dynamics provides a rigorous but seldom applied criterion for defining LLPS *in vivo*. In previous studies, where molecular diffusion was measured by spaSPT, the lack of differences in diffusion dynamics inside versus outside a presumed LLPS compartment revealed that the compartment was actually not formed by LLPS (Collombet et al, 2021; McSwiggen et al, 2019a). Here, by measuring diffusion of EWS::FLI1 in the nucleolus versus the nucleoplasm, we found that it diffuses much more slowly in the nucleolus, as expected of this well-studied, bone fide LLPS compartment. This observation provides a proof of concept that spaSPT measurements of protein diffusion rates can serve as an effective means for detecting LLPS based on differential viscosities within live cells. The fact that LLPS causes differences in molecular diffusion is likely important for cellular functions. For example, putative LLPS of TAF15 LCD not only causes a redistribution of EWS::FLI1 and transcription machinery as discussed above (Figure 5B) but also possibly con-

finer diffusion of transcription regulators and potentially alters their diffusion behaviors within the TAF15 LCD puncta. It remains unknown how such changes in protein dynamics at target genes affect transactivation, and future studies are required to reveal potential functional consequences.

Limitations of the study

A technical limitation in this study is that our method for single-molecule diffusion measurements cannot precisely quantify diffusion rates within small puncta, e.g., TAF15 LCD puncta that often fall in the submicron range. In the absence of quantitative evidence for LLPS, we refrained from concluding that the TAF15 LCD puncta are true LLPS condensates, although we observed apparent LLPS of TAF15 LCD based on prominent droplet-like behaviors (McSwiggen et al, 2019b). Our inability to measure diffusion dynamics within submicron puncta stems from the following limitations: (1) it is often ambiguous whether a single-molecule localization falls within a punctum or above/below it, given that the depth of our focal volume (Tokunaga et al, 2008) is larger than the puncta, (2) because the puncta are small compared with the diffraction limit of light, it is difficult to precisely define their boundaries in images and to localize molecules near boundaries, (3) the puncta drift in position over time, making it difficult to distinguish their overall motion from molecular diffusion within them, and (4) it is difficult to distinguish slow diffusion inside the puncta from stable binding with localization error, which is considerable given the small puncta sizes.

A conceptual limitation in our study stems from the fact that EWS::FLI1 specifically recognizes not only GGAA microsatellites but also a non-repetitive canonical ETS (Erythroblast Transformation Specific) TF binding sequence (Mao et al, 1994). Whereas the ETS-binding sequence is known to be associated with some EWS::FLI1 target genes (Siligan et al, 2005), it is unknown whether EWS::FLI1 activates these genes by forming hubs like what it does at GGAA-affiliated genes and whether multivalent LCD-LCD interactions are essential for transactivation here. Carrying out the type of super-resolution live-cell imaging reported here for genes with a single non-repetitive TF-binding site poses challenges beyond the current technical capabilities that generally limit the field. We thus have not investigated genes associated with a single canonical ETS-binding site and have restricted our analysis to EWS::FLI1 target genes that are associated with GGAA microsatellites in this study.

STAR★METHODS

Detailed methods are provided in the online version of this paper and include the following:

- KEY RESOURCES TABLE
- RESOURCE AVAILABILITY
 - Lead contact
 - Materials availability
 - Data and code availability
- EXPERIMENTAL MODEL AND SUBJECT DETAILS
- METHOD DETAILS
 - Stable cell line construction
 - Fluorescence in situ hybridization (FISH)

- Confocal fluorescence imaging and analyses for protein and nucleic acid distribution
- Flow cytometry analyses of protein expression levels
- Fluorescence recovery after photobleaching (FRAP)
- Stroboscopic photo-activatable single particle tracking (spaSPT) and analyses
- RT-qPCR and analyses
- xCELLigence assay
- Soft agar colony formation assay
- **QUANTIFICATION AND STATISTICAL ANALYSIS**

SUPPLEMENTAL INFORMATION

Supplemental information can be found online at <https://doi.org/10.1016/j.molcel.2022.04.007>.

ACKNOWLEDGMENTS

We thank L. Lavis for providing fluorescent HaloTag ligands; Q. Zhu for help with molecular cloning; K. Adiga for help optimizing conditions of doxycycline induction; S. Irgen-Giorgio for help performing flow cytometry; the CRL Flow Cytometry Facility and Molecular Imaging Center; the Caltech Flow Cytometry Facility and Biological Imaging Center; and A. Hansen, S. Teves, Q. Han, and members of the Tjian/Darzacq labs for critical reading of the manuscript. This work was supported by the John D. Baldeschwieler and Marlene R. Konnar Foundation (to S.C.), the Jane Coffin Childs Memorial Fund for Medical Research (to T.G.W.G.), California Institute of Regenerative Medicine grant LA1-08013 (to X.D.), NIH grants U01-EB021236 and U54-DK107980 (to X.D.), and the Howard Hughes Medical Institute (to R.T.).

AUTHOR CONTRIBUTIONS

Conceptualization, R.T. and S.C.; funding acquisition, R.T., X.D., C.D.-D., S.C., and T.G.W.G.; investigation, S.C., T.G.W.G., C.D.-D., G.M.D., and R.T.; software: S.C. and T.G.W.G.; visualization, S.C., T.G.W.G., and C.D.-D.; project administration, R.T. and S.C.; writing – original draft, S.C., R.T., T.G.W.G., and C.D.-D.; writing – review & editing, S.C., R.T., T.G.W.G., C.D.-D., and X.D.; supervision, R.T.

DECLARATION OF INTERESTS

R. Tjian and X. Darzacq are co-founders of Eikon Therapeutics.

Received: September 16, 2021

Revised: February 14, 2022

Accepted: April 1, 2022

Published: April 27, 2022

REFERENCES

Banani, S.F., Lee, H.O., Hyman, A.A., and Rosen, M.K. (2017). Biomolecular condensates: organizers of cellular biochemistry. *Nat. Rev. Mol. Cell Biol.* **18**, 285–298.

Boehning, M., Dugast-Darzacq, C., Rankovic, M., Hansen, A.S., Yu, T., Marie-Nelly, H., McSwiggan, D.T., Kokic, G., Dailey, G.M., Cramer, P., et al. (2018). RNA polymerase II clustering through carboxy-terminal domain phase separation. *Nat. Struct. Mol. Biol.* **25**, 833–840.

Boeynaems, S., Alberti, S., Fawzi, N.L., Mittag, T., Polymenidou, M., Rousseau, F., Schymkowitz, J., Shorter, J., Wolozin, B., Van Den Bosch, L., et al. (2018). Protein phase separation: a new phase in cell biology. *Trends Cell Biol.* **28**, 420–435.

Boija, A., Klein, I.A., Sabari, B.R., Dall’Agnese, A., Coffey, E.L., Zamudio, A.V., Li, C.H., Shrinivas, K., Manteiga, J.C., Hannett, N.M., et al. (2018). Transcription factors activate genes through the phase-separation capacity of their activation domains. *Cell* **7**, 1842–1855.e16.

Boulay, G., Sandoval, G.J., Riggi, N., Iyer, S., Buisson, R., Naigles, B., Awad, M.E., Rengarajan, S., Volorio, A., McBride, M.J., et al. (2017). Cancer-specific retargeting of BAF complexes by a prion-like domain. *Cell* **171**, 163–178.e19.

Bracha, D., Walls, M.T., Wei, M.T., Zhu, L., Avalos, J.L., Toettcher, J.E., and Brangwynne, C.P. (2019). Mapping local and global liquid phase behavior in living cells using photo-oligomerizable seeds. *Cell* **1–2**, 407.

Brangwynne, C.P., Mitchison, T.J., and Hyman, A.A. (2011). Active liquid-like behavior of nucleoli determines their size and shape in *Xenopus laevis* oocytes. *Proc. Natl. Acad. Sci. USA* **108**, 4334–4339.

Cho, W.K., Spille, J.H., Hecht, M., Lee, C., Li, C., Grube, V., and Cisse, I.I. (2018). Mediator and RNA polymerase II clusters associate in transcription-dependent condensates. *Science* **361**, 412–415.

Chong, S., Dugast-Darzacq, C., Liu, Z., Dong, P., Dailey, G.M., Cattoglio, C., Heckert, A., Banala, S., Lavis, L., Darzacq, X., and Tjian, R. (2018). Imaging dynamic and selective low-complexity domain interactions that control gene transcription. *Science* **361**, eaar2555. <https://doi.org/10.1126/science.aar2555>.

Chong, S., and Mir, M. (2021). Towards decoding the sequence-based grammar governing the functions of intrinsically disordered protein regions. *J. Mol. Biol.* **433**, 166724.

Collombet, S., Rall, I., Dugast-Darzacq, C., Heckert, A., Halavatyi, A., Le Saux, A., Dailey, G., Darzacq, X., and Heard, E. (2021). RNA polymerase II depletion from the inactive X chromosome territory is not mediated by physical compartmentalization. Preprint at bioRxiv. <https://doi.org/10.1101/2021.03.26.437188>.

Dufourt, J., Trullo, A., Hunter, J., Fernandez, C., Lazaro, J., Dejean, M., Morales, L., Nait-Amer, S., Schulz, K.N., Harrison, M.M., et al. (2018). Temporal control of gene expression by the pioneer factor Zelda through transient interactions in hubs. *Nat. Commun.* **9**, 5194.

Dynan, W.S., and Tjian, R. (1983). The promoter-specific transcription factor Sp1 binds to upstream sequences in the SV40 early promoter. *Cell* **35**, 79–87.

Elf, J., Li, G.W., and Xie, X.S. (2007). Probing transcription factor dynamics at the single-molecule level in a living cell. *Science* **316**, 1191–1194.

Gangwal, K., Sankar, S., Hollenhorst, P.C., Kinsey, M., Haroldsen, S.C., Shah, A.A., Boucher, K.M., Watkins, W.S., Jorde, L.B., Graves, B.J., and Lessnick, S.L. (2008). Microsatellites as EWS/FLI response elements in Ewing’s sarcoma. *Proc. Natl. Acad. Sci. USA* **105**, 10149–10154.

Grimm, J.B., English, B.P., Choi, H., Muthusamy, A.K., Mehl, B.P., Dong, P., Brown, T.A., Lippincott-Schwartz, J., Liu, Z., Lionnet, T., and Lavis, L.D. (2016). Bright photoactivatable fluorophores for single-molecule imaging. *Nat. Methods* **13**, 985–988.

Guillon, N., Tirode, F., Boeva, V., Zynovyyev, A., Barillot, E., and Delattre, O. (2009). The oncogenic EWS-FLI1 protein binds *in vivo* GGAA microsatellite sequences with potential transcriptional activation function. *PLoS One* **4**, e4932.

Guo, Y.E., Manteiga, J.C., Henninger, J.E., Sabari, B.R., Dall’Agnese, A., Hannett, N.M., Spille, J.H., Afeyan, L.K., Zamudio, A.V., Shrinivas, K., et al. (2019). Pol II phosphorylation regulates a switch between transcriptional and splicing condensates. *Nature* **572**, 543–548.

Hansen, A.S., Pustova, I., Cattoglio, C., Tjian, R., and Darzacq, X. (2017). CTCF and cohesin regulate chromatin loop stability with distinct dynamics. *eLife* **6**, e25776. <https://doi.org/10.7554/eLife.25776>.

Hansen, A.S., Woringer, M., Grimm, J.B., Lavis, L.D., Tjian, R., and Darzacq, X. (2018). Robust model-based analysis of single-particle tracking experiments with Spot-On. *eLife* **7**, e33125. <https://doi.org/10.7554/eLife.33125>.

Harlow, M.L., Maloney, N., Roland, J., Guillen Navarro, M.J., Easton, M.K., Kitchen-Goosen, S.M., Boguslawski, E.A., Madaj, Z.B., Johnson, B.K., Bowman, M.J., et al. (2016). Lurbinectedin inactivates the Ewing sarcoma oncoprotein EWS-FLI1 by redistributing it within the nucleus. *Cancer Res.* **76**, 6657–6668.

Heckert, A., Dahal, L., Tjian, R., and Darzacq, X. (2021). Recovering mixtures of fast diffusing states from short single particle trajectories. Preprint at bioRxiv. <https://doi.org/10.1101/2021.05.03.442482>.

- Henninger, J.E., Oksuz, O., Shrinivas, K., Sagi, I., LeRoy, G., Zheng, M.M., Andrews, J.O., Zamudio, A.V., Lazaris, C., Hannett, N.M., et al. (2021). RNA-mediated feedback control of transcriptional condensates. *Cell* **184**, 207–225.e24.
- Hnisz, D., Shrinivas, K., Young, R.A., Chakraborty, A.K., and Sharp, P.A. (2017). A phase separation model for transcriptional control. *Cell* **169**, 13–23.
- Johnson, K.M., Mahler, N.R., Saund, R.S., Theisen, E.R., Taslim, C., Callender, N.W., Crow, J.C., Miller, K.R., and Lessnick, S.L. (2017a). Role for the EWS domain of EWS/FLI in binding GGAA-microsatellites required for Ewing sarcoma anchorage independent growth. *Proc. Natl. Acad. Sci. USA* **114**, 9870–9875.
- Johnson, K.M., Taslim, C., Saund, R.S., and Lessnick, S.L. (2017b). Identification of two types of GGAA-microsatellites and their roles in EWS/FLI binding and gene regulation in Ewing sarcoma. *PLoS One* **12**, e0186275.
- Kadonaga, J.T., Courey, A.J., Ladika, J., and Tjian, R. (1988). Distinct regions of Sp1 modulate DNA binding and transcriptional activation. *Science* **242**, 1566–1570.
- Kwon, I., Kato, M., Xiang, S., Wu, L., Theodoropoulos, P., Mirzaei, H., Han, T., Xie, S., Corden, J.L., and McKnight, S.L. (2013). Phosphorylation-regulated binding of RNA polymerase II to fibrous polymers of low-complexity domains. *Cell* **155**, 1049–1060.
- Lessnick, S.L., Dacwag, C.S., and Golub, T.R. (2002). The Ewing's sarcoma oncoprotein EWS/FLI induces a p53-dependent growth arrest in primary human fibroblasts. *Cancer Cell* **1**, 393–401.
- Mao, X., Miesfeldt, S., Yang, H., Leiden, J.M., and Thompson, C.B. (1994). The FLI-1 and chimeric EWS-FLI-1 oncoproteins display similar DNA binding specificities. *J. Biol. Chem.* **269**, 18216–18222.
- McSwiggen, D.T., Hansen, A.S., Teves, S.S., Marie-Nelly, H., Hao, Y., Heckert, A.B., Umemoto, K.K., Dugast-Darzacq, C., Tjian, R., and Darzacq, X. (2019a). Evidence for DNA-mediated nuclear compartmentalization distinct from phase separation. *eLife* **8**, e4709. <https://doi.org/10.7554/eLife.47098>.
- McSwiggen, D.T., Mir, M., Darzacq, X., and Tjian, R. (2019b). Evaluating phase separation in live cells: diagnosis, caveats, and functional consequences. *Genes Dev.* **33**, 1619–1634.
- Mir, M., Reimer, A., Haines, J.E., Li, X.Y., Stadler, M., Garcia, H., Eisen, M.B., and Darzacq, X. (2017). Dense bicoid hubs accentuate binding along the morphogen gradient. *Genes Dev.* **31**, 1784–1794.
- Mir, M., Stadler, M.R., Ortiz, S.A., Hannon, C.E., Harrison, M.M., Darzacq, X., and Eisen, M.B. (2018). Dynamic multifactor hubs interact transiently with sites of active transcription in *Drosophila* embryos. *eLife* **7**, e40497. <https://doi.org/10.7554/eLife.40497>.
- Mitrea, D.M., Cika, J.A., Guy, C.S., Ban, D., Banerjee, P.R., Stanley, C.B., Nourse, A., Deniz, A.A., and Kriwacki, R.W. (2016). Nucleophosmin integrates within the nucleolus via multi-modal interactions with proteins displaying R-rich linear motifs and rRNA. *eLife* **5**, e13571. <https://doi.org/10.7554/eLife.13571>.
- Mitrea, D.M., Cika, J.A., Stanley, C.B., Nourse, A., Onuchic, P.L., Banerjee, P.R., Phillips, A.H., Park, C.G., Deniz, A.A., and Kriwacki, R.W. (2018). Self-interaction of NPM1 modulates multiple mechanisms of liquid-liquid phase separation. *Nat. Commun.* **9**, 842.
- Narlikar, G.J., Myong, S., Larson, D., Maeshima, K., Francis, N., Rippe, K., Sabari, B., Strader, L., and Tjian, R. (2021). Is transcriptional regulation just going through a phase? *Mol. Cell* **81**, 1579–1585.
- Oka, S., Shiraishi, Y., Yoshida, T., Ohkubo, T., Sugiura, Y., and Kobayashi, Y. (2004). NMR structure of transcription factor Sp1 DNA binding domain. *Biochemistry* **43**, 16027–16035.
- Randolph, L.N., Bao, X., Zhou, C., and Lian, X. (2017). An all-in-one, Tet-On 3G inducible PiggyBac system for human pluripotent stem cells and derivatives. *Sci. Rep.* **7**, 1549.
- Riback, J.A., Zhu, L., Ferrolino, M.C., Tolbert, M., Mitrea, D.M., Sanders, D.W., Wei, M.T., Kriwacki, R.W., and Brangwynne, C.P. (2020). Composition-dependent thermodynamics of intracellular phase separation. *Nature* **581**, 209–214.
- Sabari, B.R., Dall'Agnese, A., Boija, A., Klein, I.A., Coffey, E.L., Shrinivas, K., Abraham, B.J., Hannett, N.M., Zamudio, A.V., Manteiga, J.C., et al. (2018). Coactivator condensation at super-enhancers links phase separation and gene control. *Science* **361**, eaar3958. <https://doi.org/10.1126/science.aar3958>.
- Schneider, C.A., Rasband, W.S., and Eliceiri, K.W. (2012). NIH Image to ImageJ: 25 years of image analysis. *Nat. Methods* **9**, 671–675.
- Schneider, N., Wieland, F.G., Kong, D., Fischer, A.A.M., Hörner, M., Timmer, J., Ye, H., and Weber, W. (2021). Liquid-liquid phase separation of light-inducible transcription factors increases transcription activation in mammalian cells and mice. *Sci. Adv.* **7**, eabd3568. <https://doi.org/10.1126/sciadv.abd3568>.
- Shin, Y., Berry, J., Pannucci, N., Haataja, M.P., Toettcher, J.E., and Brangwynne, C.P. (2017). Spatiotemporal control of intracellular phase transitions using light-activated optoDroplets. *Cell* **168**, 159–171.e14.
- Shin, Y., and Brangwynne, C.P. (2017). Liquid phase condensation in cell physiology and disease. *Science* **357**, eaaf4382. <https://doi.org/10.1126/science.aaf4382>.
- Shin, Y., Chang, Y.C., Lee, D.S.W., Berry, J., Sanders, D.W., Ronceray, P., Wingreen, N.S., Haataja, M., and Brangwynne, C.P. (2019). Liquid nuclear condensates mechanically sense and restructure the genome. *Cell* **16**, 1518.
- Siligan, C., Ban, J., Bachmaier, R., Spahn, L., Kreppel, M., Schaefer, K.L., Poremba, C., Aryee, D.N., and Kovar, H. (2005). EWS-FLI1 target genes recovered from Ewing's sarcoma chromatin. *Oncogene* **24**, 2512–2524.
- Solovei, I., and Cremer, M. (2010). 3D-FISH on cultured cells combined with immunostaining. *Methods Mol. Biol.* **659**, 117–126.
- Sprague, B.L., Pego, R.L., Stavreva, D.A., and McNally, J.G. (2004). Analysis of binding reactions by fluorescence recovery after photobleaching. *Biophys. J.* **86**, 3473–3495.
- Tokunaga, M., Imamoto, N., and Sakata-Sogawa, K. (2008). Highly inclined thin illumination enables clear single-molecule imaging in cells. *Nat. Methods* **5**, 159–161.
- Trojanowski, J., Frank, L., Rademacher, A., Grigaitis, P., and Rippe, K. (2021). Transcription activation is enhanced by multivalent interactions independent of phase separation. Preprint at bioRxiv. <https://doi.org/10.1101/2021.01.27.428421>.
- Wei, M.T., Chang, Y.C., Shimobayashi, S.F., Shin, Y., Strom, A.R., and Brangwynne, C.P. (2020). Nucleated transcriptional condensates amplify gene expression. *Nat. Cell Biol.* **22**, 1187–1196.
- Witzel, F., Fritsche-Guenther, R., Lehmann, N., Sieber, A., and Blüthgen, N. (2015). Analysis of impedance-based cellular growth assays. *Bioinformatics* **31**, 2705–2712.
- Xiang, L., Chen, K., Yan, R., Li, W., and Xu, K. (2020). Single-molecule displacement mapping unveils nanoscale heterogeneities in intracellular diffusivity. *Nat. Methods* **17**, 524–530.
- Zuo, L., Zhang, G., Massett, M., Cheng, J., Guo, Z., Wang, L., Gao, Y., Li, R., Huang, X., Li, P., and Qi, Z. (2021). Loci-specific phase separation of FET fusion oncoproteins promotes gene transcription. *Nat. Commun.* **12**, 1491.

STAR★METHODS

KEY RESOURCES TABLE

REAGENT or RESOURCE	SOURCE	IDENTIFIER
Chemicals, peptides, and recombinant proteins		
Doxycycline	Sigma	D3447
Deposited data		
Raw confocal imaging and FRAP data	This paper; Zenodo	https://doi.org/10.5281/zenodo.6052378
Raw single-molecule imaging data	This paper; Zenodo	https://doi.org/10.5281/zenodo.6050687
Raw images of confocal fluorescence microscopy and soft agar colony formation assays shown in the figures	This paper; Mendeley Data	http://doi.org/10.17632/3mn3wbnmw6.1
Experimental models: Cell lines		
Human: A673 carrying HaloTag knock-in at the <i>ews::fli1</i> locus	Chong et al., 2018	N/A
Human: knock-in A673 with inducible expression of mNG-EWS-NPM1	This paper	N/A
Human: knock-in A673 with inducible expression of mNG-NPM1	This paper	N/A
Oligonucleotides		
RNA FISH probes targeting <i>ABHD6</i> , see Table S1	LGC Biosearch Technologies	N/A
RNA FISH probes targeting <i>CAV1</i> , see Table S1	LGC Biosearch Technologies	N/A
RNA FISH probes targeting <i>GAPDH</i>	LGC Biosearch Technologies	ISMF-2151-5
DNA FISH probes	This paper	N/A
Recombinant DNA		
Plasmid: mNG-EWS	This paper	N/A
Plasmid: EGFP-TAF15	This paper	N/A
Plasmid: mNG-EWS-NPM1	This paper	N/A
Plasmid: mNG-NPM1	This paper	N/A
Software and algorithms		
ImageJ	Schneider et al., 2012	https://imagej.nih.gov/ij/
Protein colocalization analysis codes	Chong et al., 2018 ; GitHub	https://github.com/Shasha-Chong/CodeFor2018SciencePaper
Quot	Heckert et al., 2021 ; GitHub	https://github.com/alecheckert/quot
Spot-On	Hansen et al., 2018	https://spoton.berkeley.edu
Codes for analyzing diffusion dynamics in and out of the nucleolus	This paper; GitLab	https://gitlab.com/tjian-darzacq-lab/nucleolar-spt-analysis

RESOURCE AVAILABILITY

Lead contact

Further information and requests for resources and reagents should be directed to and will be fulfilled by the lead contact, Robert Tjian (jmlim@berkeley.edu).

Materials availability

Plasmids and cell lines generated in this study will be shared by the lead contact upon request.

Data and code availability

- Original microscopy data has been deposited at Zenodo and Mendeley Data and is publicly available as of the date of publication. DOIs are listed in the [key resources table](#).
- All codes for spaSPT data analyses have been submitted to GitLab and are publicly available (<https://gitlab.com/tjian-darzacq-lab/nucleolar-spt-analysis>).
- Any additional information required to reanalyze the data reported in this paper is available from the lead contact upon request.

EXPERIMENTAL MODEL AND SUBJECT DETAILS

The knock-in A673 cell line expressing endogenous EWS::FLI1-Halo (Chong et al, 2018) were grown in high-glucose DMEM (Thermo Fisher, 10566016) with 10% FBS and 1% penicillin-streptomycin. The sex of the cell line is female. For live-cell imaging, the medium was identical except that phenol-red-free DMEM (ThermoFisher, 31053028) was used. The knock-in cells and those with modifications described in the “stable cell line construction” section were cultured at 37°C with 5% CO₂.

METHOD DETAILS

Stable cell line construction

We engineered the knock-in A673 line to express high levels of mNG-EWS-NPM1 or mNG-NPM1 upon doxycycline induction using PiggyBac transposition, drug selection, and clone selection. First, we cloned the cDNA encoding mNG-EWS-NPM1 or mNG-NPM1 into an Xlone vector (Randolph et al, 2017) containing PiggyBac elements, a Tet-On 3G inducible gene expression system, and a puromycin resistance gene. We then co-transfected the knock-in cells with the Xlone vector and a SuperPiggyBac transposase vector using Lipofectamine 3000 transfection reagent (ThermoFisher Scientific, L300015) following the manufacturer’s instructions. 72 hours after transfection, we started with selection by adding 1 μg/ml puromycin. Untransfected knock-in cells were treated with puromycin in parallel, and selection was judged to be complete once no untransfected cells remained (~3 days). To make a clonal cell line with sufficiently high induction of mNG-EWS-NPM1 to sequester endogenous EWS::FLI1-Halo to the nucleolus, we plated the puromycin-selected cells one cell per well into 96-well plates by limiting dilution, expanded single clones, and screened for clones by fluorescence imaging with a high-throughput automated confocal microscope (Perkin Elmer, Opera Phenix, 40x water objective). To prepare for live-cell imaging samples, we plated clones in 96-well plates (Perkin Elmer, CellCarrier-96), induce expression of mNG-EWS-NPM1 with doxycycline (100~200 ng/ml) for 96 hours, stain cells with 200 nM JF646 HaloTag ligand for 15 min, and washed twice (each wash: remove medium, rinse twice with PBS, incubate in fresh medium for 30 min). At the end of the final wash, the medium was changed to phenol-red-free imaging medium as described above. After identifying a desirable clonal cell line with high induction of mNG-EWS-NPM1, we isolated single clones of puromycin-selected cells with inducible expression of mNG-NPM1 and used a flow cytometer (BD Biosciences, BD LSRFortessa Cell Analyzer) to screen for clones with mNG-NPM1 levels similar to mNG-EWS-NPM1 as described above under the same induction condition (Figure S4A).

Fluorescence in situ hybridization (FISH)

The knock-in A673 cells were plated on 18 mm circular No. 1 cover glasses (VWR VistaVision, 16004-300) and transfected with a protein expression plasmid using Lipofectamine 3000. 24 hours after transfection, we stained the cells with 200 nM JFX549 HaloTag ligand following the protocol described above, fixed the cells, and then proceeded with FISH. To measure nascent transcription levels of *ABHD6*, *CAV1*, and *GAPDH* genes, we performed intron RNA FISH following the published Stellaris RNA FISH protocol for adherent cells (https://biosearchassets.blob.core.windows.net/assets/bti_stellaris_protocol_adherent_cell.pdf) using Quasar 670-labeled FISH probes purchased from LGC Biosearch Technologies. We purchased predesigned FISH probes targeting the intron of *GAPDH* (LGC Biosearch Technologies, ISMF-2151-5). We designed FISH probes targeting the introns of *ABHD6* and *CAV1* using the online software Stellaris Probe Designer (<https://www.biosearchtech.com/support/tools/design-software/stellaris-probe-designer>). The sequences of FISH probes targeting *ABHD6* and *CAV1* are listed in Table S1. To visualize *ABHD6* and *CAV1* gene loci with DNA FISH, we prepared FISH probes targeting each gene following the procedure described in (Solovei and Cremer, 2010) and performed 3D DNA FISH following the published protocol.

Confocal fluorescence imaging and analyses for protein and nucleic acid distribution

Two confocal microscopes were used to image intron RNA FISH samples. One is an inverted laser scanning confocal microscope (Zeiss, LSM 710 AxioObserver) equipped with 34-channel spectral detection, a motorized stage, a full incubation chamber maintaining 37°C and 5% CO₂, a heated stage, an X-Cite 120 illumination source as well as several laser lines (405, 458, 488, 514, 561, 591, 633 nm). Images were acquired with a 40x Plan NeoFluar NA1.3 oil-immersion objective under control of the Zeiss Zen software. The other is an inverted laser scanning confocal microscope with Airyscan super-resolution capability (Zeiss, LSM 900 with Airyscan 2) and equipped with four laser lines (405, 488, 561, 640 nm). Images were acquired with a 40x oil objective (Zeiss Plan-Apochromat 40x/1.3 Oil DIC) in the confocal (CO) mode under control of the Zen software. We acquired z stacks of RNA FISH samples with a slice interval of 0.3 μm. 405 nm, 488 nm, 561 nm, and 633 or 640 nm lasers were used to excite the fluorescence of Hoechst-labeled nuclei, EGFP or mNG-labeled proteins, JFX549-labeled EWS::FLI1-Halo, and Quasar 670-labeled intron RNA FISH, respectively. Before acquiring any fluorescence image, we carefully set the laser intensity and microscope detectors to make sure that no pixel in the image was saturated. We used proper emission filters for sequential four-color imaging and ensured no bleed-through between the four channels by imaging cell samples that contain only one of the four fluorophores (Hoechst, EGFP or mNG, JFX549, and Quasar 670) under the four-color imaging settings. To quantify intron RNA FISH intensities, we used ImageJ (Schneider et al., 2012) to make z projection for each z stack that results in a sum intensity image, integrated the intensity of all pixels within a gene locus on the sum image, and subtracted the product of the average intranuclear background intensity and the pixel number within the gene locus. In box plots involving nuclear fluorescent protein intensities (Figures 1D–1F, 2E–2G, 3C–3E, S1A, S1D, S1E, S1H, S1I, S2A,

S2D–S2G, and S3D–S3G), the intensities were the average intranuclear intensities on the sum images generated from z projection of the protein z-stack images. To measure the integrated EWS::FLI1-Halo intensity at each *ABHD6* or *CAV1* gene locus (Figures S1H, S1I, S2F, and S2G), we identified location of a gene locus in the RNA FISH z stack in 3D (the number of the z-stack slice where the gene locus has the highest integrated FISH intensity and the central pixel of the locus on that slice), selected the same location in 3D in the corresponding EWS::FLI1-Halo z stack, and integrated the EWS::FLI1-Halo intensity of all pixels within an area ($0.68 \mu\text{m} \times 0.68 \mu\text{m}$) that centers the selected pixel on the selected slice.

DNA FISH samples were imaged on the confocal microscope (Zeiss, LSM 900 with Airyscan 2) in the super-resolution (SR) mode using the 40x oil objective described above. We acquired z stacks of DNA FISH samples with a slice interval of $0.2 \mu\text{m}$. 405 nm, 488 nm, and 640 nm lasers were used to excite the fluorescence of Hoechst-labeled nuclei, EGFP-TAF15, and Cy5-labeled DNA FISH, respectively. We made sure no pixel in the image was saturated and there was no bleed-through between three channels using the approaches described above.

For live-cell imaging of fluorescent protein distribution (Figures 1A, 2A, and 3A), the knock-in A673 cells were grown on glass-bottom (No. 1.5, 14 mm diameter) 35 mm dishes (MatTek, P35G-1.5-14-C), transfected with a protein expression plasmid using Lipofectamine 3000, and stained the cells with 200 nM JF646 or JFX549 HaloTag ligand. The live-cell samples were imaged on the Airyscan confocal microscope in the super-resolution (SR) mode using the 40x oil objective. We acquired z stacks of the samples with a slice interval of $0.2 \mu\text{m}$. We made sure no pixel in the image was saturated and there was no bleed-through between channels. Protein enrichment at the endogenous EWS::FLI1-Halo hubs (Figures 1B, 2B, and S3H) was examined by image analysis methods described in (Chong et al, 2018). Radial intensity profiles were plotted using a published ImageJ plugin “Radial Profile Plot” (<https://imagej.nih.gov/ij/plugins/radial-profile.html>).

Flow cytometry analyses of protein expression levels

The knock-in A673 cells were transfected with the mNG-EWS or EGFP-TAF15 expression plasmid using Lipofectamine 3000. 24 hours after transfection, we stained the cells with 200 nM JFX646 HaloTag ligand following the protocol described above. We then measured the fluorescence intensities of JFX646-labeled EWS::FLI1-Halo (excited with the 638 nm laser) and mNG-EWS or EGFP-TAF15 (excited with the 488 nm laser) of single cells using a flow cytometer (Beckman Coulter, CytoFLEX) to make box plots of EWS::FLI1-Halo intensities in the presence of different intensities of mNG-EWS (Figure S1B) or EGFP-TAF15 (Figure S2B). To examine potential bleed-through of fluorescence from the green to red channel, we used the above flow cytometry settings to measure the knock-in A673 cells that are transfected with the mNG-EWS or EGFP-TAF15 expression plasmid but not stained with the JFX646 HaloTag ligand. We observed no increase in the baseline fluorescence of the red channel when mNG-EWS or EGFP-TAF15 is expressed at all levels, suggesting no bleed-through from the green to red channel.

Fluorescence recovery after photobleaching (FRAP)

FRAP was performed on the inverted laser scanning confocal microscope (Zeiss, LSM 710 AxioObserver) described above. The 561 nm laser and the epi-illumination mode were used for FRAP measurements. Images were acquired with a 40x Plan NeoFluar NA1.3 oil-immersion objective. The knock-in A673 cells were grown on glass-bottom (No. 1.5, 14 mm diameter) 35 mm dishes (MatTek, P35G-1.5-14-C). To measure the FRAP dynamics of EWS::FLI1-Halo in the nucleolus, we transfected the knock-in cells with a plasmid encoding mNG-EWS-NPM1 and stained the cells with 500 nM HaloTag TMR ligand (Promega, G8251) following the protocol described above. We acquired 1000 frames at one frame per 0.3 seconds with the first 5 frames acquired before the bleach pulse for the measurement of baseline fluorescence of the bleach spot and the whole nucleus. We chose to photobleach a circular spot with a radius of $1 \mu\text{m}$ within a nucleolus using the 561 nm laser at maximum intensity. We extracted FRAP curves from the acquired movies using methods described in (Chong et al, 2018). To measure the FRAP dynamics of EWS::FLI1-Halo in the nucleoplasm, we followed the same procedure as above, except that the knock-in cells were not transfected and a circular bleach spot with a radius of $1 \mu\text{m}$ was chosen within the nucleoplasm of a cell and at least $1 \mu\text{m}$ from nuclear and nucleolar boundaries. We found the FRAP dynamics of EWS::FLI1-Halo in the nucleolus and the nucleoplasm were dependent on the bleach spot size (data not shown), suggesting that both diffusion and molecular interaction dynamics significantly contributed to the observed FRAP dynamics and neither could be quantified by fitting the FRAP curves to analytical models (Sprague et al, 2004).

Stroboscopic photo-activatable single particle tracking (spaSPT) and analyses

The knock-in cells with inducible expression of mNG-EWS-NPM1 were grown on 25 mm circular No. 1.5 cover glasses (Azer Scientific, 200251) that were plasma-cleaned prior to use. We induced the cells with 200 ng/ml of doxycycline for 96 hours, stained the cells with 20 nM PA-JF646 and 200 nM JFX549 HaloTag ligands, and performed single-molecule imaging of EWS::FLI1-Halo on a custom-built Nikon (Nikon Instruments Inc.) TI microscope described in (Hansen et al, 2017). We took images with a 100x/NA 1.49 oil-immersion TIRF objective (Nikon apochromat CFI Apo TIRF 100x Oil) under highly inclined and laminated optical sheet (HILO) illumination (Tokunaga et al, 2008) using following laser lines: 488 nm for mNG; 561 nm for JFX549; 405 nm and 633 nm for photo-activation and excitation of PA-JF646, respectively. The incubation chamber maintained a humidified 37°C atmosphere with 5% CO_2 and the objective was similarly heated to 37°C for live-cell experiments.

High-concentration JFX549 staining allows visualization of the intracellular distribution of EWS::FLI1-Halo. We chose cells with EWS::FLI1-Halo significantly enriched in the nucleolus to perform spaSPT (Figure 4B). The procedure of spaSPT largely follows

what is described in (Hansen et al, 2017). Both the excitation laser (633 nm) and the photo-activation laser (405 nm) for PA-JF646 were pulsed. Each frame consisted of a 7-ms camera exposure time followed by a ~ 500 μ s camera 'dead' time. The excitation laser (633 nm) was pulsed for 1 ms starting at the beginning for the 7 ms camera exposure time. The photo-activation laser (405 nm) was pulsed during the ~ 500 μ s camera 'dead' time, minimizing fluorescence background. Each cell was imaged for 20,000 frames corresponding to ~ 1.5 min. We recorded movies for 20 cells per day for 4 days. Over 400,000 single EWS::FLI1-Halo molecules were localized and tracked using the `quot` package (<https://github.com/alecheckert/quot>) (Heckert et al, 2021). All the downstream analysis was performed using custom MATLAB code.

To prepare binary masks of nuclei and nucleoli, images of mNG-EWS-NPM1 collected before and after each single-molecule movie were first averaged and then filtered using Gaussian filters of width 1.5 pixels for nucleoli and 5 pixels for nuclei. Filtered images were then binarized using the threshold

$$T = I_{min} + A(I_{max} - I_{min})$$

where I_{min} and I_{max} are the minimum and maximum pixel intensities and A is a constant, which was set to 0.05 for nuclei and 0.3 for nucleoli. These binary masks were used to classify each single-molecule localization as nucleolar, nucleoplasmic, or cytoplasmic. Trajectories were classified as nucleolar or nucleoplasmic if all localizations in that trajectory fell within the nucleolus or nucleoplasm, respectively (Figure 4C). Sorted trajectories from multiple cells were pooled by subnuclear compartment and fit to a 2-state model using Spot-On (Hansen et al, 2018) with parameters listed in Table S2. Bootstrap confidence intervals for fit parameters were determined by randomly resampling data by cell with replacement. Spot-On was used to analyze 200 bootstrap replicates, and a 95% confidence interval was estimated as the mean value of each parameter plus or minus 1.96 standard deviations.

Randomized nucleolar masks were prepared using a sequence of 10000 Monte Carlo moves (Figure S5A). At each step, each nucleolus (i.e., connected component in the nucleolar mask) was displaced horizontally by -1, 0, or +1 pixels, displaced vertically by -1, 0, or +1 pixels, and rotated by -10° , 0° , or $+10^\circ$. Each displacement or rotation was set to occur with an equal probability. Alternatively, "teleportation" to a new random location within the nuclear mask was performed with a probability of 1% per step. This new configuration was accepted if all nucleoli remained within the nucleus and did not overlap, and it was rejected otherwise. The current configuration was written out every 100 steps. Spot-On was used to analyze a total of 200 randomized mask replicates. For each replicate, one randomized mask was chosen per cell from Monte Carlo steps 1000 and above. Sorting of nucleolar and nucleoplasmic trajectories and analysis using Spot-On was performed as described above.

RT-qPCR and analyses

Total RNA was purified from cells (treated or not with 150 ng/mL of doxycycline for 96 hours) using Trizol (Thermo Fisher Scientific, 15596026) and quantified by Nanodrop. 500 ng of total RNA was retrotranscribed to cDNA using Maxima First Strand cDNA Synthesis Kit for RT-qPCR, with dsDNase (Thermo Fisher Scientific, K1671). 5 μ l of 1:20 cDNA dilutions were used for quantitative PCR with SYBR Select Master Mix for CFX (Applied Biosystems, ThermoFisher) on a BIO-RAD CFX Real-time PCR system. Two biological replicates and three technical replicates for each were performed for each gene. To normalize the data, we used the average value of 4 invariant transcripts (*GAPDH*, *MED12*, *NAE1*, *BGALT3*) (Chong et al, 2018) (Figure S4B) and calculated the normalized fold change for each target gene (Figure 3F). Primers used were as described in (Chong et al, 2018).

xCELLigence assay

The Cell Index (a representation of cell growth and viability) was measured in real time using the xCELLigence real-time cell analysis (RTCA) single plate instrument (RTCA-SP) (Acea Biosciences) following manufacturer's instructions. Cells were seeded at a density of 4000 cells/well in an RTCA E-plate View 96 (Agilent, 300601010). After 24 hours, protein expression (mNG-NPM1 or mNG-EWS-NPM1) was induced by replacing the media with fresh media containing 150 ng/mL of doxycycline. Media was changed every 48 days afterwards. The Cell Index (graphed as Cell Number in Figure S4C) was normalized to the value measured 7 hours after induction for each condition.

Soft agar colony formation assay

To examine how induction of mNG-EWS-NPM1 or mNG-NPM1 affects the malignant transformation phenotype of the knock-in A673 cells, we first seeded cells at a density of 6×10^4 per well in a 6-well plate in 0.4% SeaPlaque GTG agarose (Fisher, BMA50111) and IMDM (ThermoFisher, 12200036) medium containing 20% FBS and 1% penicillin-streptomycin, added 0.3 ml liquid media (IMDM with 10% FBS and 1% penicillin-streptomycin) per well on top of agar, and cultured the cells in agar at 37°C with 5% CO_2 for 5 days. Then we induced protein expression by replacing the liquid media with new medium containing doxycycline that corresponds to 25 ng/ml in the entire cell culture volume (agar and liquid). We cultured the cells at 37°C with 5% CO_2 for another 10 days, changing doxycycline-containing liquid media every 3 days, and then stained the cells by applying to each well 200 μ l of 1 mg/ml nitro blue tetrazolium chloride (NBT, Thermo Fisher, N6495) in PBS. After culturing the stained cells in agar for 24 hours, we took images of the wells with a ChemiDoc MP imaging system (Bio-Rad). The live colonies appeared as distinct dots on agar (Figure 3G). We counted the number of sizable colonies (diameter > 220 μ m) for quantitative analyses. Inducible knock-in cells were cultured in agar without doxycycline induction in parallel. Two biological replicates and three technical replicates for each were performed for each condition. The average number of induced colonies is divided by the average number

of uninduced colonies to calculate the fold change by protein induction. The fold changes by induction of mNG-EWS-NPM1 and mNG-NPM1 are plotted in [Figure 3H](#).

QUANTIFICATION AND STATISTICAL ANALYSIS

We used MATLAB to perform two-sample t-tests for statistical comparison of two groups of single-cell data. A one-tailed p-value below 0.05 demonstrates significant difference. Error bars in [Figures 4A](#) and [S4A–S4C](#) represent standard deviations. Error bars in [Figure 3H](#) represent standard errors. The sample sizes for error calculations are provided in respective figure legends and [method details](#). To calculate the error bar for each condition in [Figures 1G](#), [S1F](#), and [S1G](#), we used the bootstrap method to generate 2000 resampled image sets from each original set of mNG-EWS or intron RNA FISH images centering the gene loci, calculated the integrated fluorescence intensity at the gene loci ($0.68 \mu\text{m} \times 0.68 \mu\text{m}$ area) of each image set and then the standard deviation of the mean values. We took the bootstrapped mean value as the test statistic and performed two-sample t-tests to calculate p-values.